High-order upwind schemes for the wave equation on overlapping grids: Maxwell's equations in second-order form

Jordan B. Angel[a,1,2,3], Jeffrey W. Banks[a,1,2,4,*], William D. Henshaw[a,1,2]

[a]*Department of Mathematical Sciences, Rensselaer Polytechnic Institute, Troy, NY 12180, USA*

Abstract

High-order accurate upwind approximations for the wave equation in second-order form on overlapping grids are developed. Although upwind schemes are well established for first-order hyperbolic systems, it was only recently shown by Banks and Henshaw [1] how upwinding could be incorporated into the second-order form of the wave equation. This new upwind approach is extended here to solve the time-domain Maxwell's equations in second-order form; schemes of arbitrary order of accuracy are formulated for general curvilinear grids. Taylor time-stepping is used to develop single-step space-time schemes, and the upwind dissipation is incorporated by embedding the exact solution of a local Riemann problem into the discretization. Second-order and fourth-order accurate schemes are implemented for problems in two and three space dimensions, and overlapping grids are used to treat complex geometry and problems with multiple materials. Stability analysis of the upwind-scheme on overlapping grids is performed using normal mode theory. The stability analysis and computations confirm that the upwind scheme remains stable on overlapping grids, including the difficult case of thin boundary grids when the traditional non-dissipative scheme becomes unstable. The accuracy properties of the scheme are carefully evaluated on a series of classical scattering problems for both perfect conductors and dielectric materials in two and three space dimensions. The upwind scheme is shown to be robust and provide high-order accuracy.

Keywords: wave equations, electromagnetics, upwind methods, overlapping grids

Contents

1 Introduction **2**

2 Overlapping grids **4**

3 Upwind flux on a curvilinear grid **6**

4 Upwind approximations on curvilinear and overlapping grids **7**
4.1 The space-time upwind scheme 8
4.2 Discrete approximation formula for some flux terms 11
4.3 Choosing the time-step 12

5 Stability for wave equations on overlapping grids **12**
5.1 Stability and convergence for thin boundary grids 13

*Corresponding author

Email addresses: angelj2@rpi.edu (Jordan B. Angel), banksj3@rpi.edu (Jeffrey W. Banks), henshw@rpi.edu (William D. Henshaw)

[1]This work was partially funded by the DARPA Defense Sciences Office.

[2]This work was partially performed under DOE contracts from the ASCR Applied Math Program.

[3]This work was partially performed under DOD contract W911NF-14-C-0161.

[4]Research supported by a U.S. Presidential Early Career Award for Scientists and Engineers.

5.2 Normal mode analysis for overlapping grids . . . 15
5.3 Grid parameter space search for unstable modes . . . 19

6 Numerical Results **22**
6.1 Scattering from a perfectly conducting cylinder . . . 23
6.2 Scattering from a dielectric cylinder . . . 25
6.3 Scattering from a perfectly conducting sphere . . . 27
6.4 Scattering from a dielectric sphere . . . 27
6.5 Scattering of a chirped plane wave from a conducting body embedded in a dielectric slab . . . 30

7 Conclusions **32**

Appendix A Computational grids **33**
Appendix A.1 Composite grid for a disk . . . 33
Appendix A.2 Composite grid for the exterior of a two-dimensional cylinder . . . 34
Appendix A.3 Composite grid for a dielectric disk embedded in a square domain . . . 34
Appendix A.4 Composite grid for the region exterior to a sphere . . . 35
Appendix A.5 Composite grid for a dielectric sphere embedded in a box . . . 36
Appendix A.6 Composite grid for a rectangular shaped body embedded in a dielectric slab . . . 36

1. Introduction

Partial differential equations governing wave propagation problems are typically formulated in either first-order form as a first-order hyperbolic system, or in second-order form (e.g. the classical wave equation $u_{tt} = c^2\Delta u$). As discussed in [1], treating the second-order form directly can often have a number of advantages. For example, there may be fewer dependent variables (e.g. going from six to three dependent variables for Maxwell's equations) and in some cases fewer constraint equations (e.g. the Saint-Venant compatibility conditions for linear elasticity written in first-order form). An additional advantage of the second-order form is that it is straight-forward to develop compact, high-order accurate, and discretely self-adjoint approximations to the Laplace operator [2]. In contrast, the first-order form often requires the use of staggered grids for finite difference methods [3], or special edge elements for finite-element methods [4] to avoid nontrivial null-spaces, which can lead to numerical difficulties in the form of undamped or growing highly oscillatory modes.

Until recently, one significant advantage of using the first-order system form of the equations has been the availability of robust and accurate numerical schemes based on upwinding, or more generally schemes which incorporate the characteristic structure of the PDE into the discrete operators. The first instance of such a scheme is the one developed by Courant, Isaacson, and Rees [5], which was built around the idea of characteristics but did not directly invoke the idea of "upwind". It was the landmark 1959 paper of Godunov [6] which spoke of directly incorporating upwinding by embedding the exact solution of the Riemann problem into the numerical technique. The core idea in this approach is that the solution to the Riemann problem correctly accounts for the directional transport, the so-called wind, of characteristic quantities. Based on these fundamental ideas there have been many powerful extensions including for example, the flux-corrected transport method [7], semi-Lagrangian methods [8–10], the piecewise-parabolic-method (PPM) [11], essentially-non-oscillatory (ENO) schemes [12, 13], discontinuous Galerkin (DG) methods [14], and weighted-essentially-non-oscillatory (WENO) methods [15]. In fact, as discussed in [16], there exists a direct relationship between upwind numerical methods and schemes that directly incorporate an artificial dissipation; such artificial dissipation schemes are still in wide-spread use and trace their origins to the artificial viscosity scheme of Richtmeyer and von Neumann [17–19]. However, there are significant advantages of directly using ideas of upwinding, as opposed to ad-hoc addition of an artificial dissipation, in that the form and scaling of the dissipation in upwind schemes is a natural by-product of the method and as a result it is not necessary to tune artificial parameters or the form of the dissipation operators.

Despite their success for the first-order system, upwind methods directly applicable to wave equations posed in second-order form were not discussed until recently in [1]. The key idea introduced in [1], which was essentially similar to the original approach of Godunov [6], was based on embedding the well-known

d'Alembert solution into the discretization. This d'Alembert solution plays a similar role to the Riemann problem for the first-order system and provides a mechanism to account for the wave nature of the solution. Following the established procedure for upwind treatments for the first-order form, a localized expression of the upwind flux was derived that enables easy application to a wide class of problems including those in multiple space dimensions and those with variable coefficients. In [1], schemes with order-of-accuracy ranging from 1 to 6 were developed and the numerical approximations were found to be quite well behaved even for very difficult problems involving weak solutions with jumps; a particularly difficult case for the second-order form of the equations. Subsequently in [20], a preliminary extension of the scheme to overlapping grids was performed. Similar to the experience with upwind methods for the first-order system, the second-order system upwind methods were found to be stabilizing even for difficult cases involving overlapping grids where dissipation-free schemes for wave equations are known to exhibit instabilities [21]. Recently, a similar construction was followed to develop discontinuous Galerkin methods for the second-order form of the equations in [22].

Maxwell's equations in the time-domain are usually solved in first-order form and there are a wide class of methods that have been developed for their solution, including those based on finite difference, spectral, pseudo-spectral, finite-element, and discontinuous Galerkin, amongst others. The literature is very broad; for a good introduction see, for example, the review by Hestaven [23] or the references in the books by Taflove [24] and Cohen [25]. Note also that overlapping grids have previously been used for the solution of Maxwell's equations in first order form by Driscoll and Fornberg [26] using a hybrid pseudo-spectral finite-difference scheme. Despite the many excellent schemes that have been developed, there still remains a need in some applications for more efficient schemes on complex geometries that are both robust and high-order accurate. Toward this end, a scheme based on upwind schemes (for robustness) and overlapping grids (for efficiency) may prove to be useful. Therefore, in the current work we extend the ideas for high-order upwind methods outlined in [1, 20] to discretize Maxwell's equations in second-order form on overlapping grids. In this framework, geometric complexity introduced by both physical boundaries (e.g. perfectly conducting boundaries) and interfaces between dielectric materials will be treated using composite overlapping grids. A simple motivating example, which involves the interaction of an impinging electromagnetic wave on one perfectly conducting disk and one dielectric disk, is illustrated in Fig. 1. As in [2], the governing equations

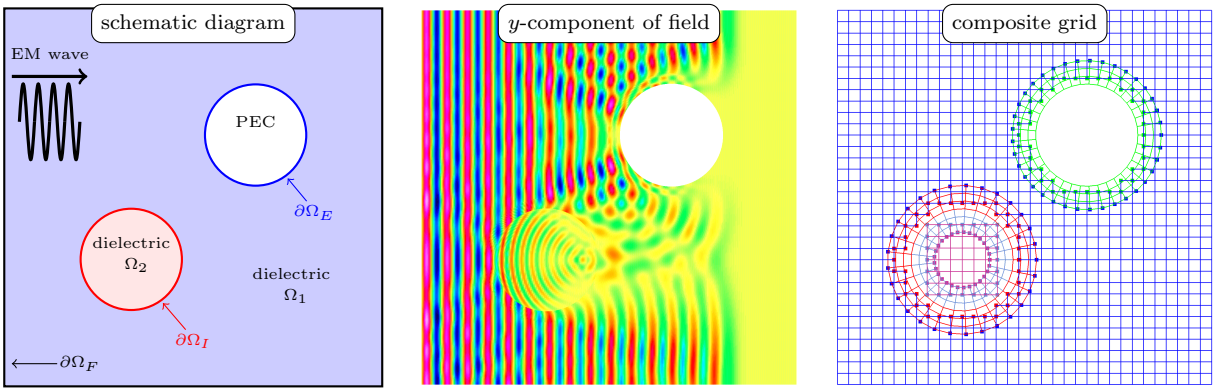

Figure 1: Motivating example illustrating electromagnetic diffraction of a plane wave from a dielectric disk and a perfectly conducting disk. The left figure provides a schematic of the problem, the middle figure shows the y-component of the electric field from an actual computation, and the right figure shows a coarse version of a composite grid suitable for computation with the second-order accurate scheme.

are written as a system of scalar wave equations for the components of the electric field which are coupled at domain boundaries and material interfaces. In contrast to [2] which relies on a simple artificial dissipation, we achieve stabilization against overlapping grid instabilities through the use of upwind discretizations. As will be demonstrated, these upwind discretizations are stable for all overlapping grid configurations investigated without any adjustable artificial viscosity. This is true even for the difficult case where the boundary fitted grids use a fixed number of grid points as the composite grid is refined. For such a refinement process the overlapping grid interpolation boundary approaches the physical boundary with the result that overlapping

grid instabilities become more pronounced [21]. This situation is theoretically investigated here in one dimension using the normal mode stability theory of Gustafsson, Kreiss, and Sundström [27, 28], and the upwind dissipation is found to be stabilizing. Indeed the upwind discretizations are evidently stable and accurate in higher dimensions even for refinements that yield thin boundary grids. On the other hand the artificial dissipation approach in [2] requires an increasingly large artificial viscosity parameter which results in a reduction in observed accuracy.

As discussed above, our motivation is the study of the propagation of electromagnetic waves in domains consisting of one or more distinct materials. Such a scenario is depicted in Fig. 1, which illustrates the interaction of an incident electromagnetic wave propagating through a background dielectric material (blue in the schematic and labeled Ω_1) with two cylindrical inclusions; the first cylinder being comprised of a material with different dielectric properties than the background (red in the schematic and labeled Ω_2), and the second cylinder being a perfect electrical conductor (PEC) (white in the schematic). The entire domain of interest is the union of the subdomains associated with each material, $\Omega = \Omega_1 \cup \Omega_2$ in this case. Boundaries are then identified by type with $\partial\Omega_E$ indicating an external PEC boundary, $\partial\Omega_I$ a material interface separating dielectrics, and $\partial\Omega_F$ a far-field truncation. As in [2], each material is assumed to have a constant electrical permittivity, ϵ, and constant magnetic permeability, μ, and it is assumed that there are no external charges or currents. In this setting, Maxwell's equations can be formulated as the second-order system for the electric field vector $\mathbf{E}(\mathbf{x}, t) \in \mathbb{R}^d$ in d space dimensions,

$$\partial_t^2 \mathbf{E} = c^2 \Delta \mathbf{E}, \qquad \mathbf{x} \in \Omega, \tag{1a}$$

$$\mathbf{n} \times \mathbf{E} = 0, \quad \nabla \cdot \mathbf{E} = 0, \qquad \mathbf{x} \in \partial\Omega_E, \quad \text{(PEC BC's)} \tag{1b}$$

$$[\mathbf{n} \times \mathbf{E}]_I = 0, \quad [\epsilon \mathbf{n} \cdot \mathbf{E}]_I = 0, \qquad \mathbf{x} \in \partial\Omega_I, \quad \text{(interface conditions)} \tag{1c}$$

$$\mathcal{B}_F(\mathbf{E}) = 0, \quad \nabla \cdot \mathbf{E} = 0, \qquad \mathbf{x} \in \partial\Omega_F, \quad \text{(far field BC's)} \tag{1d}$$

$$\mathbf{E}(\mathbf{x}, 0) = \mathbf{E}^{(0)}(\mathbf{x}), \quad \mathbf{E}_t(\mathbf{x}, 0) = \mathbf{E}_t^{(0)}(\mathbf{x}). \qquad \text{(initial conditions)} \tag{1e}$$

Here $c = 1/\sqrt{\epsilon\mu}$ is the wave speed which is constant for each dielectric material, $\mathbf{n}$ is the normal vector to the boundary or interface, and $[\cdot]_I$ represents the jump across the interface Ω_I. Where the domain is truncated, the far field boundary condition is denoted by $\mathcal{B}_F(\mathbf{E}) = 0$. Further details concerning the derivation of (1a)-(1e) from the more common first-order formulation can be found in [2].

The remainder of this manuscript is arranged as follows. Section 2 introduces our formulation on overlapping grids, and Section 3 briefly describes the derivation of the upwind flux for curvilinear grids. Section 4 then describes the overall upwind discretizations used for overlapping grids. The stability of the upwind scheme on overlapping grids for the difficult case of thin boundary grids is considered in Section 5. A normal mode analysis is performed on a one-dimensional overlapping grid and the resulting stability conditions are checked through a numerical parameter search. Numerical results are presented in Section 6 which include classical scattering problems from a conducting cylinder, dielectric cylinder, conducting sphere, and dielectric sphere. A final result showing scattering from a buried conducting object using an incident field with time-dependent frequency is also included. Concluding remarks are given in Section 7, while Appendix A gives precise descriptions of all the overlapping grids used in the computations.

2. Overlapping grids

As discussed in Section 1, the governing Maxwell's equations are cast as a system of scalar wave equations whose components are coupled only along physical boundaries or interfaces between disparate materials. On domain interiors then, the components of the fields satisfy the classical wave equation

$$\frac{\partial^2 u}{\partial t^2} = Lu, \qquad \mathbf{x} \in \Omega, \tag{2a}$$

$$L \stackrel{\text{def}}{=} c^2 \Delta = c^2 \sum_{\mu=1}^{d} \frac{\partial^2}{\partial x_\mu^2}, \tag{2b}$$

where $\mathbf{x} \in R^d$, $u = u(\mathbf{x}, t)$ is a component of the electric or magnetic field, d is the physical dimension of the problem, and Δ is the Laplacian operator in d dimensions. The focus of the current work is to discretize (2a)

using an overlapping grid approach where the overall domain is covered by an overlapping grid $\mathcal{G}$ consisting of a set of component grids G_k on which the discrete solutions are coupled through interpolation. Such a scenario is depicted in Fig. 2 which shows a domain consisting of an annular grid (green) and a rectangular grid (blue). In the region where these two grids overlap the solution is communicated from one grid to the other using interpolation. For further details on overlapping grids refer to [29] and the references therein. Also note that boundary and interface conditions are applied using *ghost points* following the discussion in [2] with one slight modification. For a scheme with order of accuracy $p = 2, 4, 6, \ldots$, the discretizations described in this work have a stencil width of $p+3$ instead of the stencil width $p+1$ used in [2], and as a result one additional ghost point is needed at boundaries and interpolation interfaces. For the results presented here, values at these additional ghost points are obtained by $p+1$ order extrapolation.

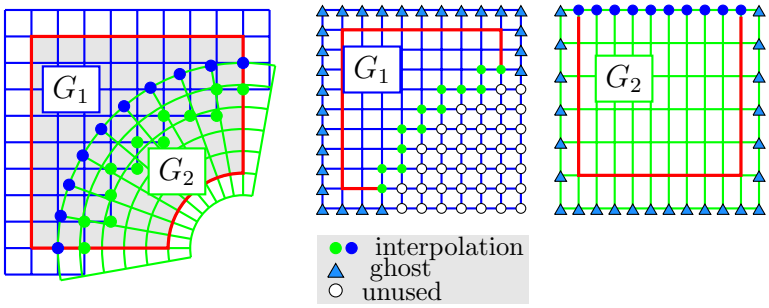

Figure 2: Left: an overlapping grid consisting of two structured curvilinear component grids, $\mathbf{x} = G_1(\mathbf{r})$ and $\mathbf{x} = G_2(\mathbf{r})$. Middle and right: component grids for the square and annular grids in the unit square parameter space $\mathbf{r}$. Grid points are classified as discretization points, interpolation points or unused points. Ghost points are used to apply boundary conditions.

Each component grid of the overlapping grid is defined by a smooth invertible mapping $\mathbf{x} = \mathbf{G}(\mathbf{r})$ where $\mathbf{r} \in [0,1]^d$ denotes the unit parameter-space coordinate-vector in d space dimensions. The governing equations will be transformed from physical space, $\mathbf{x} = [x_1, x_2, x_3]^T$, to parameter space, $\mathbf{r} = [r_1, r_2, r_3]^T$. Note that a dependent variable such as u can be regarded as a function of either $\mathbf{x}$ or $\mathbf{r}$. To differentiate between the two we will use lower case for dependence on $\mathbf{x}$, as in $u(\mathbf{x}, t)$, and upper case for $\mathbf{r}$, as in $U(\mathbf{r}, t)$, with $U(\mathbf{r}, t) = u(G(\mathbf{r}), t)$. Following [2], the operator $L = c^2\Delta$ can be written in *conservation form* for a general curvilinear mapping as

$$Lu = \frac{1}{J} \sum_{l=1}^{d} \frac{\partial F_l}{\partial r_l}, \tag{3a}$$

where $F_l = F_l(\mathbf{r}, t)$ is the flux function in the parameter-space coordinate direction r_l given by

$$F_l \stackrel{\text{def}}{=} \sum_{m=1}^{d} J\, \mathcal{R}^{lm} \frac{\partial U}{\partial r_m}, \tag{3b}$$

$$\mathcal{R}^{lm} \stackrel{\text{def}}{=} c^2 \sum_{\mu=1}^{d} \frac{\partial r_l}{\partial x_\mu} \frac{\partial r_m}{\partial x_\mu}, \tag{3c}$$

and where J is the determinant of the Jacobian matrix $\partial\mathbf{x}/\partial\mathbf{r} = [\partial x_i/\partial r_j]$. Note that in (3a), the conserved quantity is Ju, and the metrics of the mapping enter the equation as variable coefficients. Each component grid is represented discretely using a logically rectangular grid, so that in the computational space coordinates $\mathbf{r}$ the grid will be rectangular with grid spacing h_l in the r_l direction. Grid functions will be denoted by $w_{\mathbf{i}}$ where $\mathbf{i} = [i_1, i_2, i_3]$ is a multi-index. Note that we use D_{+l}, D_{-l}, and D_{0l} to denote the usual forward, backward and central divided-difference operators in coordinate direction r_l, defined by

$$D_{+l} w_{\mathbf{i}} \stackrel{\text{def}}{=} \frac{w_{\mathbf{i}+\mathbf{e}_l} - w_{\mathbf{i}}}{h_l}, \quad D_{-l} w_{\mathbf{i}} \stackrel{\text{def}}{=} \frac{w_{\mathbf{i}} - w_{\mathbf{i}-\mathbf{e}_l}}{h_l}, \quad D_{0l} w_{\mathbf{i}} \stackrel{\text{def}}{=} \frac{w_{\mathbf{i}+\mathbf{e}_l} - w_{\mathbf{i}-\mathbf{e}_l}}{2h_l},$$

where $\mathbf{e}_l$ is the unit vector in coordinate direction l, for example $\mathbf{e}_2 = [0,1,0]^T$. These operators are also for continuous functions by

$$D_{+l}U(\mathbf{r}) \stackrel{\text{def}}{=} \frac{U(\mathbf{r}+\mathbf{h}_l) - U(\mathbf{r})}{h_l}, \quad D_{-l}U(\mathbf{r}) \stackrel{\text{def}}{=} \frac{U(\mathbf{r}) - U(\mathbf{r}-\mathbf{h}_l)}{h_l}, \quad D_{0l}U(\mathbf{r}) \stackrel{\text{def}}{=} \frac{U(\mathbf{r}+\mathbf{h}_l) - U(\mathbf{r}-\mathbf{h}_l)}{2h_l}.$$

3. Upwind flux on a curvilinear grid

In this section we first review the original derivation of upwinding for the second-order wave equation as discussed in [1], and then subsequently extend that work to derive the form of the upwinding terms on curvilinear grids. In [1], the upwind contribution for use with Cartesian grids was derived from the d'Alembert solution to a generalized Riemann problem with left state $(u_{x,L}, v_L)$ for $x < 0$ and right state $(u_{x,R}, v_R)$ for $x > 0$ where v denotes the velocity $v = u_t$. For positive times, the d'Alembert solution reveals that the spatial derivative u_x is constant at $x = 0$, and this value is taken as the "upwind" state $\overset{*}{u}_x$ given by

$$\overset{*}{u}_x = \frac{1}{2}(u_{x,L} + u_{x,R}) + \frac{1}{2c}(v_R - v_L).$$

It was shown in [1] that the second term involving the jump in the velocity provides the upwinding, and ultimately the dissipation in the scheme. As a result, u_x was taken to be continuous and the upwind state was ultimately given as

$$\overset{*}{u}_x = u_x + \frac{1}{2c}(v_R - v_L). \tag{4}$$

As we subsequently realized, not surprisingly the same upwind state can alternatively be derived from the solution to a classical Riemann problem for the first-order system formulation of the equations. This latter approach is now followed in deriving the upwind flux for curvilinear grids.

In order to more clearly understand the general derivation of the upwind state for the wave equation, the first-order system in one dimension is expressed using the classical formulation based on velocity $v = u_t$ and stress $\sigma = \rho c^2\, u_x$ as

$$\rho v_t = \sigma_x, \tag{5a}$$
$$\sigma_t = \rho c^2\, v_x. \tag{5b}$$

The density ρ, as appears for example in solid mechanics, has been included in this description since it is useful in the coming discussion and helps to clarify the physical interpretation[5]. Based on a characteristic analysis, the upwind state for the flux σ arising from the solution to a Riemann problem in the first-order system is

$$\overset{*}{\sigma} = \frac{1}{2}\left(\sigma_L + \sigma_R\right) + \frac{z}{2}\left(v_R - v_L\right),$$

where (v_m, σ_m), $m = L, R$ are the left and right states, and $z = \rho c$ is the impedance. As before, the stress is assumed continuous and the upwind flux reduces to

$$\overset{*}{\sigma} = \sigma + \frac{\rho c}{2}(v_R - v_L). \tag{6}$$

Note that equation (6) is essentially the same as (4), but importantly differs in that the upwind state is expressed in terms of the stress rather than simply the spatial derivative u_x.

On a curvilinear grid, the wave equation is written in a mapped space as given in equations (3a)-(3c). The relevant terms in the corresponding first-order system formulation for waves traveling in the r_l direction are then given by

$$(\rho J)\, v_t = \sigma_{r_l}, \tag{7a}$$
$$\sigma_t = (\rho J)\, \mathcal{R}^{ll}\, v_{r_l}, \tag{7b}$$

[5]For electromagnetics in the second-order form, the correspondence is $\rho \to \mu$, $v \to \partial_t E$, $\sigma \to \mu c^2 \partial_x E$, $\rho c \to \sqrt{\mu/\epsilon}$.

where $\sigma = (\rho J)\,\mathcal{R}^{ll}\,u_{r_l}$. The terms appearing in (7a)-(7b) are those that will contribute to the solution of the Riemann problem with a initial jump in the r_l-direction. Comparing (7a)-(7b) to (5a)-(5b) we see that ρJ takes the place of the density in (5a)-(5b) and $\mathcal{R}^{ll} = c^2\|\nabla_{\mathbf{x}} r_l\|^2$ takes the place of the sound-speed squared. It follows that the upwind flux on a curvilinear grid for waves propagating in direction r_l takes the form (corresponding to equation (6))

$$\begin{aligned}\overset{*}{\sigma} &= \sigma + \frac{1}{2}\,\frac{\rho J\sqrt{\mathcal{R}^{ll}}}{2}\,(v_R - v_L),\\ &= (\rho J)\mathcal{R}^{ll}u_{r_l} + \frac{\rho J\sqrt{\mathcal{R}^{ll}}}{2}\,(v_R - v_L).\end{aligned} \tag{8}$$

Note that a mapped impedance could be identified as $\mathcal{Z}^l = \rho J\sqrt{\mathcal{R}^{ll}}$. Equation (8) is the key condition that will be used to incorporate upwinding into the approximations defined in Section 4. It is important to point out that the form (8) remains valid whether $J > 0$ or $J < 0$, and therefore the upwind scheme remains robust to right-handed vs. left-handed grid transformations.

4. Upwind approximations on curvilinear and overlapping grids

In this section, we will develop high-order accurate upwind discretizations for the wave equation (2b) on general curvilinear grids. These schemes will subsequently be applied to solving Maxwell's equations on overlapping grids and it will be demonstrated that the schemes remain stable on overlapping grids even in the difficult case when the boundary fitted grids have a fixed number of grid points in the normal direction as the grid is refined.

To develop approximations of different orders of accuracy we follow the procedure in [1] and express the governing equations in curvilinear coordinates in an exact *discrete conservation form*

$$\begin{aligned}\frac{\partial^2 U}{\partial t^2} = LU(\mathbf{r},t) &\overset{\text{def}}{=} \frac{1}{J}\sum_{l=1}^{d} D_{-l}\, f_l(\mathbf{r}+\mathbf{h}_l/2,t)\\ &= \frac{1}{J}\sum_{l=1}^{d}\frac{f_l(\mathbf{r}+\mathbf{h}_l/2,t) - f_l(\mathbf{r}-\mathbf{h}_l/2,t)}{h_l}.\end{aligned} \tag{9}$$

Here the conserved quantity is Ju since the local area element scales with J, and the flux functions f_l at grid faces $\mathbf{r}\pm\mathbf{h}_l/2$ are defined in terms of the fluxes F_l, defined in (3b), and a linear operator $\mathcal{S}_{h_l}$ defined by

$$f_l(\mathbf{r},t) \overset{\text{def}}{=} \mathcal{S}_{h_l}\left[F_l(\mathbf{r},t)\right]. \tag{10}$$

Importantly the functions f_l and operator $\mathcal{S}_{h_l}$ will be defined so that (9) is identical to the original wave equation with L defined from (3a). The operator $\mathcal{S}_{h_l}$ depends on h_l and satisfies the identity

$$\frac{\partial F_l}{\partial r_l}(\mathbf{r},t) \overset{\text{def}}{=} D_{-l} f_l(\mathbf{r}+\mathbf{h}_l/2,t) = D_{-l}\mathcal{S}_{h_l}F_l(\mathbf{r}+\mathbf{h}_l/2,t), \tag{11}$$

for any sufficiently smooth function F_l. Therefore, $\mathcal{S}_{h_l}$ is given by the expansion

$$\mathcal{S}_{h_l} = \sum_{j=0}^{\infty}\alpha_j\, h_l^{2j}\frac{\partial^{2j}}{\partial r_l^{2j}} \;= I - \frac{h_l^2}{24}\frac{\partial^2}{\partial r_l^2} + \frac{7h_l^4}{5760}\frac{\partial^4}{\partial r_l^4} - \frac{31h_l^6}{967680}\frac{\partial^6}{\partial r_l^6} + \dots\,. \tag{12}$$

The coefficients α_j in (12) can be computed from the identity $\zeta/2 = \sinh(\zeta/2)\sum_{j=0}^{\infty}\alpha_j\zeta^{2j}$ by equating coefficients of ζ in the Taylor series expansion, following the approach described in [30, 31]. As in [1], the time derivative of the field quantity U is introduced, indicated using a dot as in $\dot{U}\equiv\frac{\partial U}{\partial t}$, and the governing equations are expressed as

$$\frac{\partial}{\partial t}\begin{bmatrix}U\\ \dot{U}\end{bmatrix} = \frac{1}{J}\begin{bmatrix}\dot{U}\\ \sum_{l=1}^{d}\partial_r F_l\end{bmatrix}. \tag{13}$$

Equations (13) are integrated over a time step Δt, to produce the formally exact differential-difference equations

$$\dot{U}(\mathbf{r}, t^{n+1}) = \dot{U}(\mathbf{r}, t^n) + \frac{\Delta t}{J} \sum_{l=1}^{d} D_{-l}\, \mathcal{F}_l^{\dot{u}}(\mathbf{r} + \frac{\mathbf{h}_l}{2}, t^n), \tag{14a}$$

$$U(\mathbf{r}, t^{n+1}) = U(\mathbf{r}, t^n) + \Delta t\, \dot{U}(\mathbf{r}, t^n) + \frac{\Delta t^2}{J} \sum_{l=1}^{d} D_{-l}\, \mathcal{F}_l^{u}(\mathbf{r} + \frac{\mathbf{h}_l}{2}, t^n), \tag{14b}$$

where $t^n = n\Delta t$ denotes the time at step n while $\mathcal{F}_l^{\dot{u}}$ and $\mathcal{F}_l^{u}$ in (14a)-(14b) are defined as time-averages of the face-centered flux f_l,

$$\mathcal{F}_l^{\dot{u}}(\mathbf{r} + \frac{\mathbf{h}_l}{2}, t^n) \stackrel{\text{def}}{=} \frac{1}{\Delta t} \int_0^{\Delta t} f_l(\mathbf{r} + \frac{\mathbf{h}_l}{2}, t^n + \tau)\, d\tau, \tag{15a}$$

$$\mathcal{F}_l^{u}(\mathbf{r} + \frac{\mathbf{h}_l}{2}, t^n) \stackrel{\text{def}}{=} \frac{1}{\Delta t^2} \int_0^{\Delta t} \int_0^{\tau} f_l(\mathbf{r} + \frac{\mathbf{h}_l}{2}, t^n + \tau')\, d\tau'\, d\tau. \tag{15b}$$

Upwind dissipation is incorporated into the discretization through an appropriate choice of numerical flux function $\overset{*}{f}_l$ as an approximation to f_l. Let

$$V_l(\mathbf{r} + \frac{\mathbf{h}_l}{2}, t^n + \tau) \stackrel{\text{def}}{=} \mathcal{S}_{h_l} \left[\dot{U}\right]_{\mathbf{r}+\frac{\mathbf{h}_l}{2}}^{t^n+\tau}, \tag{16}$$

denote the quantity, proportional to the *velocity* $\dot{U}$, that appears in the jump term of equation (8). Note that square brackets, with associated subscript and superscript, have been used to indicate spatial and temporal dependence as in, for example, $[U]_r^t = U(r,t)$. This notation will henceforth be adopted to simplify many of the subsequent formulae. The upwind flux on a curvilinear grid is then defined as

$$\overset{*}{f}_l(\mathbf{r} + \frac{\mathbf{h}_l}{2}, t^n + \tau) \stackrel{\text{def}}{=} \left[f_l + \frac{J\sqrt{\mathcal{R}^{ll}}}{2} \left(V_l^R - V_l^L\right) \right]_{\mathbf{r}+\frac{\mathbf{h}_l}{2}}^{t^n+\tau} \tag{17}$$

where V_l^L is a *left biased*, V_l^R is a *right-biased* approximation to V_l. Notice that the jump term in (17) is zero at the continuous level for smooth solutions and so (14a) and (14b) remain exact when f_l is replaced with $\overset{*}{f}_l$. However at a discrete level the jump terms will be nonzero (the states V_l^L and V_l^R on either side of the face being predicted using different data) and the effect of this term will be to add numerical dissipation to the scheme, similar to dissipation that results from upwind discretizations of the equations in first-order form.

4.1. The space-time upwind scheme

In this work, the discrete scheme is a single-step space-time scheme based on expanding the flux in a Taylor series in time and then using the governing equation to eliminate even time-derivatives of U or $\dot{U}$ with spatial derivatives (e.g. $U_{tt} = LU$, $\dot{U}_{tt} = L\dot{U}$, $U_{tttt} = L^2U$, etc.). To describe the single step scheme, suppose that $U_{\mathbf{i}}^n$ and $\dot{U}_{\mathbf{i}}^n$ are given at grid points $\mathbf{x_i}$ at time t^n. The goal is then to determine $U_{\mathbf{i}}^{n+1}$ and $\dot{U}_{\mathbf{i}}^{n+1}$ at the new time based on a p-th order accurate approximation. Further, assume that $J(\mathbf{r})$ and $\mathcal{R}^{lm}(\mathbf{r})$ are known functions evaluated at the grid points in parameter space $\mathbf{r_i}$.

From the the definition (12) for $\mathcal{S}_{h_l}$, the flux f_l and velocity V_l are written as series in powers of h_l,

$$f_l(\mathbf{r} + \frac{\mathbf{h}_l}{2}, t + \tau) = \sum_{j=0}^{\infty} \alpha_j h_l^{2j} \frac{\partial^{2j}}{\partial r_l^{2j}} \sum_{m=1}^{d} \left[J\mathcal{R}^{lm} \frac{\partial U}{\partial r_m} \right]_{\mathbf{r}+\frac{\mathbf{h}_l}{2}}^{t+\tau}, \tag{18a}$$

$$V_l(\mathbf{r} + \frac{\mathbf{h}_l}{2}, t^n + \tau) = \sum_{j=0}^{\infty} \alpha_j h_l^{2j} \frac{\partial^{2j}}{\partial r_l^{2j}} \left[\dot{U}\right]_{\mathbf{r}+\frac{\mathbf{h}_l}{2}}^{t^n+\tau}. \tag{18b}$$

Also for future reference define the operator L, and its powers, acting in a curvilinear coordinate system by

$$L^\nu = \left(\frac{1}{J} \sum_l \frac{\partial}{\partial r_l} \sum_{m=1}^{d} J\mathcal{R}^{lm} \frac{\partial}{\partial r_m} \right)^\nu .$$

Note that (18a) involves terms with an odd-number of r_l-derivatives while (18b) involves terms with an even number of r_l-derivatives. As in [1] the terms in (18a) will use difference approximations which are centered on cell faces, $\mathbf{r_i} + \frac{\mathbf{h}_l}{2}$. On the other hand, the terms in (18b) will use difference approximations which are centered on cell centers $\mathbf{r_i}$, and this will result in left-biased and right-biased approximations for (18b) that are used in the upwind flux (17).

Using Taylor series in time to expand equation (18a) about the cell face $\mathbf{r_i} + \frac{\mathbf{h}_l}{2}$ and time $t = t^n$ gives

$$\begin{aligned} f_l(\mathbf{r_i} + \frac{\mathbf{h}_l}{2}, t^n + \tau) &= \sum_{j=0}^{\infty} \alpha_j h_l^{2j} \frac{\partial^{2j}}{\partial r_l^{2j}} \sum_{m=1}^{d} \left[J\mathcal{R}^{lm} \frac{\partial}{\partial r_m} \sum_{\mu=0}^{\infty} \frac{\tau^\mu}{\mu!} \frac{\partial^\mu U}{\partial t^\mu} \right]_{\mathbf{r_i}+\frac{\mathbf{h}_l}{2}}^{t^n} , \\ &= \sum_{j=0}^{\infty} \alpha_j h_l^{2j} \frac{\partial^{2j}}{\partial r_l^{2j}} \sum_{m=1}^{d} \left[J\mathcal{R}^{lm} \frac{\partial}{\partial r_m} \sum_{\nu=0}^{\infty} \left(\frac{\tau^{2\nu}}{(2\nu)!} L^\nu U + \frac{\tau^{2\nu+1}}{(2\nu+1)!} L^\nu \dot{U} \right) \right]_{\mathbf{r_i}+\frac{\mathbf{h}_l}{2}}^{t^n} , \end{aligned} \tag{19}$$

where the governing equation has been used to replace even time derivatives of U or $\dot{U}$ with spatial derivatives involving powers of L. A discrete approximation to (19) at the cell faces is then defined as

$$[f_l]_{\mathbf{i}+\frac{1}{2}\mathbf{e}_l}^{t^n+\tau} \approx f_l(\mathbf{r_i} + \frac{1}{2}\mathbf{e}_l, t^n + \tau)$$

based on the known values for $U_{\mathbf{i}}^n$ and $\dot{U}_{\mathbf{i}}^n$ at point $\mathbf{i}$ and a stencil of near-by points. For a pth-order accurate scheme, where p is an even integer, equation (19) is approximated to order p in space and time. However, this p-th order accurate scheme is not unique and different choices lead to minor differences in the final scheme and in the maximum stable time-step. For the scheme presented here the following rules are used:

1. The series in (19) is truncated and only those terms of of size $\mathcal{O}((\tau + h_l)^p)$ are retained.
2. Derivatives are approximated to an accuracy of at most p.
3. When there is a choice of stencils, the most accurate centered approximation is used.

Fig. 3 shows the form of the stencils involved in the second-order accurate upwind scheme. More details on this discretization procedure for a fourth-order accurate scheme are provided in Section 4.2.

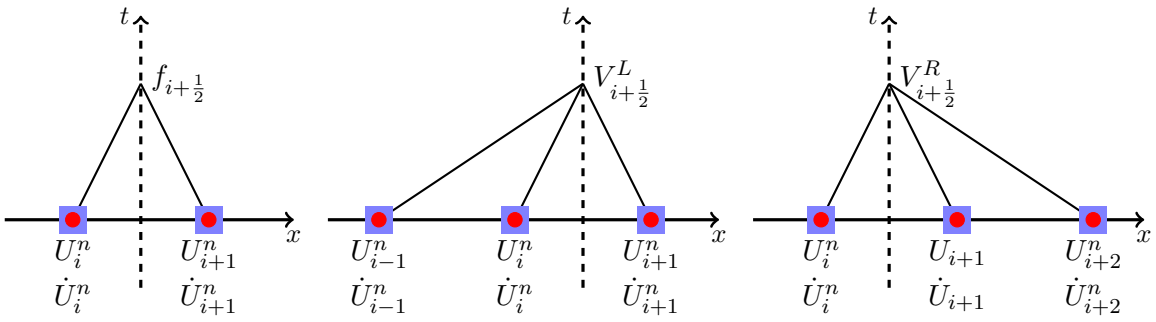

Figure 3: Geometry of the sub-stencils for the space-time upwind scheme in one dimension (second-order accuracy). Left: the stencil for the centered flux at the face, denoted by $f_{i+\frac{1}{2}}$, is two points wide and involves values of the solution U_i^n and and its time derivative $\dot{U}_i^n$. Middle and right: left-biased and right-biased contributions to the upwind flux. The overall stencil to update U_i^n and $\dot{U}_i^n$ for will be five-points wide after applying the D_- operator to the total flux.

The upwind term (18b) can also be expanded as a Taylor series in time to give

$$V_l(\mathbf{r} \pm \frac{\mathbf{h}_l}{2}, t^n + \tau) = \sum_{j=0}^{\infty} \alpha_j h_l^{2j} \frac{\partial^{2j}}{\partial r_l^{2j}} \sum_{\mu=0}^{\infty} \frac{\tau^\mu}{\mu!} \left[\frac{\partial^{\mu+1} U}{\partial t^{\mu+1}} \right]_{\mathbf{r} \pm \frac{\mathbf{h}_l}{2}}^{t^n},$$
$$= \sum_{j=0}^{\infty} \alpha_j h_l^{2j} \frac{\partial^{2j}}{\partial r_l^{2j}} \sum_{\nu=0}^{\infty} \frac{\tau^{2\nu}}{(2\nu)!} \left[L^\nu \dot{U} + \frac{\tau^{2\nu+1}}{(2\nu+1)!} L^{\nu+1} U \right]_{\mathbf{r} \pm \frac{\mathbf{h}_l}{2}}^{t^n}. \tag{20}$$

Following a common approach for generating upwind schemes, the series (20) will be further expanded as a Taylor series in space to define V_l at the cell faces $\mathbf{r_i} \pm \frac{\mathbf{h}_l}{2}$ in terms of the solution and it's derivatives defined at cell centers, $\mathbf{r_i}$,

$$V_l(\mathbf{r_i} \pm \frac{\mathbf{h}_l}{2}, t^n + \tau) = \sum_{j=0}^{\infty} \sum_{\nu=0}^{\infty} \sum_{k=0}^{\infty} \alpha_j h_l^{2j} \frac{(\pm h_l)^k}{k!} \left[\frac{\partial^{2j+k}}{\partial r_l^{2j+k}} \left(\frac{\tau^{2\nu}}{(2\nu)!} L^\nu \dot{U} + \frac{\tau^{2\nu+1}}{(2\nu+1)!} L^{\nu+1} U \right) \right]_{\mathbf{r_i}}^{t^n}. \tag{21}$$

The expansion (21) defines a left-biased approximation at the cell face $\mathbf{r_i} + \frac{\mathbf{h}_l}{2}$ and a right-biased approximation at the cell face $\mathbf{r_i} - \frac{\mathbf{h}_l}{2}$. Correspondingly, the left-biased and right-biased approximations in (17) at the cell face $\mathbf{r_i} + \frac{\mathbf{h}_l}{2}$ are given by

$$[V_l^L]_{\mathbf{i}+\frac{1}{2}\mathbf{e}_l}^{t^n+\tau} = V_l(\mathbf{r_i} + \frac{\mathbf{h}_l}{2}, t^n + \tau),$$
$$[V_l^R]_{\mathbf{i}+\frac{1}{2}\mathbf{e}_l}^{t^n+\tau} = V_l(\mathbf{r}_{\mathbf{i}+\mathbf{e}_l} - \frac{\mathbf{h}_l}{2}, t^n + \tau).$$

Note that the left-biased and right-biased approximations will in general be unequal. Given these approximations, the upwind flux (discrete in space but still continuous in τ) is defined as

$$[\overset{*}{f}_l]_{\mathbf{i}+\frac{1}{2}\mathbf{e}_l}^{t^n+\tau} \overset{\text{def}}{=} [f_l]_{\mathbf{i}+\frac{1}{2}\mathbf{e}_l}^{t^n+\tau} + \left[\frac{J\sqrt{\mathcal{R}^{ll}}}{2} \left(V_l^R - V_l^L \right) \right]_{\mathbf{i}+\frac{1}{2}\mathbf{e}_l}^{t^n+\tau}. \tag{22}$$

From (22), the upwind approximation to the time-averaged fluxes are

$$[\overset{*}{\mathcal{F}}_l^{\dot{u}}]_{\mathbf{i}+\frac{1}{2}\mathbf{e}_l}^{n} \overset{\text{def}}{=} \frac{1}{\Delta t} \int_0^{\Delta t} [\overset{*}{f}_l]_{\mathbf{i}+\frac{1}{2}\mathbf{e}_l}^{t^n+\tau} \, d\tau, \tag{23a}$$

$$[\overset{*}{\mathcal{F}}_l^{u}]_{\mathbf{i}+\frac{1}{2}\mathbf{e}_l}^{n} \overset{\text{def}}{=} \frac{1}{\Delta t^2} \int_0^{\Delta t} \int_0^{\tau} [\overset{*}{f}_l]_{\mathbf{i}+\frac{1}{2}\mathbf{e}_l}^{t^n+\tau'} \, d\tau' \, d\tau. \tag{23b}$$

The time-integrals in (23a)-(23b) can be computed exactly (since the integrands are polynomials τ or τ'). An alternative approach, the one used for the results in this paper, is to approximate the integrand by a polynomial of degree $p/2 - 1$ that interpolates the integrand at the Gauss points over the time interval $[t^n, t^{n+1}]$. This polynomial can then be integrated exactly in time. The full space-time scheme is summarized as follows.

Algorithm 1 (Space-time upwind algorithm for the wave equation on a curvilinear grid). *The updates to the discrete solution and it's time derivative are given by*

$$\dot{U}_{\mathbf{i}}^{n+1} = \dot{U}_{\mathbf{i}}^{n} + \frac{\Delta t}{J_{\mathbf{i}}} \sum_{l=1}^{d} D_{+l} \left[\overset{*}{\mathcal{F}}_l^{\dot{u}} \right]_{\mathbf{i}-\frac{1}{2}\mathbf{e}_l}^{n}, \tag{24a}$$

$$U_{\mathbf{i}}^{n+1} = U_{\mathbf{i}}^{n} + \Delta t \, \dot{U}_{\mathbf{i}}^{n} + \frac{\Delta t^2}{J_{\mathbf{i}}} \sum_{l=1}^{d} D_{+l} \left[\overset{*}{\mathcal{F}}_l^{u} \right]_{\mathbf{i}-\frac{1}{2}\mathbf{e}_l}^{n}. \tag{24b}$$

where the time-averaged fluxes $\left[\overset{*}{\mathcal{F}}_l^{\dot{u}} \right]_{\mathbf{i}-\frac{1}{2}\mathbf{e}_l}^{n}$ *and* $\left[\overset{*}{\mathcal{F}}_l^{u} \right]_{\mathbf{i}-\frac{1}{2}\mathbf{e}_l}^{n}$ *are defined by* (23a)-(23b) *which in turn use the upwind fluxes defined by* (22) *and appropriate numerical approximations to* (21) *(left and right-biased) and* (19). *More details on the numerical approximations are described in Section 4.2.*

4.2. Discrete approximation formula for some flux terms

This section provides some details of the discrete approximations used for the fourth-order accurate scheme, $p = 4$, which uses a seven point stencil. To be concrete, consider representative terms in Equation (19) for f_l, and Equation (20) for the upwind term. Approximations of face-centered values at $\mathbf{i} + \frac{1}{2}\mathbf{e}_l$ will use at most a four point stencil in the r_l direction, i.e. the stencil involves the points $[\mathbf{i}-\mathbf{e}_l, \mathbf{i}, \mathbf{i}+\mathbf{e}_l, \mathbf{i}+2\mathbf{e}_l]$. Approximations to cell-centered values at $\mathbf{i}$ (used for the upwind term) will use at most a five-point stencil in the r_l direction involving a subset of the points $[\mathbf{i} - 2\mathbf{e}_l, \mathbf{i} - \mathbf{e}_l, \ldots, \mathbf{i} + 2\mathbf{e}_l]$. The final scheme will use a forward difference of these face centered values and thus increase the final stencil width to seven. Additional details of the full approximation for the case of a Cartesian grids appears in [1].

The fourth-order accurate approximations will make use of both fourth- and second-order accurate difference and interpolation operators. Let $A^{(q)}_{+l}$ denote the discrete operator that interpolates a grid-function defined at points $\mathbf{i}$ to the face at index location $\mathbf{i} + \frac{1}{2}\mathbf{e}_l$, to an accuracy of $\mathcal{O}(h_l^q)$. For example,

$$A^{(2)}_{+l} w_{\mathbf{i}} \stackrel{\text{def}}{=} A_{+l} w_{\mathbf{i}} \stackrel{\text{def}}{=} \frac{1}{2}(w_{\mathbf{i}+\mathbf{e}_l} + w_{\mathbf{i}}), \tag{25a}$$

$$A^{(4)}_{+l} w_{\mathbf{i}} \stackrel{\text{def}}{=} A_{+l}\big(I - \frac{h_l^2}{8} D_{+l} D_{-l}\big) w_{\mathbf{i}} = \frac{9}{16}(w_{\mathbf{i}+\mathbf{e}_l} + w_{\mathbf{i}}) - \frac{1}{16}(w_{\mathbf{i}+2\mathbf{e}_l} + w_{\mathbf{i}-\mathbf{e}_l}). \tag{25b}$$

Similarly let $D^{(q)}_{+l}$ denote the q-th order-accurate approximate to the first derivative at the face location $\mathbf{r}_{\mathbf{i}} + \frac{1}{2}\mathbf{h}_l$, for example,

$$D^{(2)}_{+l} w_{\mathbf{i}} \stackrel{\text{def}}{=} D_{+l} w_{\mathbf{i}}, \tag{26a}$$

$$D^{(4)}_{+l} w_{\mathbf{i}} \stackrel{\text{def}}{=} D_{+l}\big(I - \frac{h_l^2}{24} D_{+l} D_{-l}\big) w_{\mathbf{i}}. \tag{26b}$$

Note that the first derivative at the cell face can be computed with a compact approximation (e.g. a two-point stencil gives second-order accuracy). Finally let $D^{(q)}_{0m}$ denote the standard p-th order accurate centered divided difference approximation to the first derivative at point $\mathbf{i}$, for example,

$$D^{(2)}_{0m} w_{\mathbf{i}} \stackrel{\text{def}}{=} D_{0m} w_{\mathbf{i}}, \tag{27a}$$

$$D^{(4)}_{0m} w_{\mathbf{i}} \stackrel{\text{def}}{=} D_{0m}(I - \frac{h_m^2}{6} D_{+m} D_{-m}) w_{\mathbf{i}}. \tag{27b}$$

Note that these latter approximations are not compact. In terms of these difference operators, a fourth order accurate approximation to $J\mathcal{R}^{ll}\frac{\partial u}{\partial r_l}$ on the face $\mathbf{r}_{\mathbf{i}} + \frac{1}{2}\mathbf{h}_l$ using a four-point stencil is

$$\left[J\mathcal{R}^{ll}\frac{\partial u}{\partial r_l}\right]^n_{\mathbf{i}+\frac{1}{2}\mathbf{e}_l} \approx A^{(4)}_{+l}\big(J_{\mathbf{i}}\mathcal{R}^{ll}_{\mathbf{i}}\big)\ D^{(4)}_{+l} U^n_{\mathbf{i}}. \tag{28}$$

Terms in (19) with coefficient τ^2 need only be approximated to second-order accuracy in space,

$$\left[J\mathcal{R}^{ll}\frac{\tau^2}{2}\frac{\partial L}{\partial r_l} U\right]^n_{\mathbf{i}+\frac{1}{2}\mathbf{e}_l} \approx A^{(2)}_{+l}\big(J_{\mathbf{i}}\mathcal{R}^{ll}_{\mathbf{i}}\big)\ \frac{\tau^2}{2} D^{(2)}_{+l}\big(L^{(2)} U^n_{\mathbf{i}}\big), \tag{29}$$

where $L^{(2)}U_{\mathbf{i}}$ denotes a second-order accurate difference approximation to Lu at $\mathbf{r}_{\mathbf{i}}$. Terms involving mixed derivatives use centered approximations in the transverse directions and these approximations are interpolated to the face at $\mathbf{i} + \frac{1}{2}\mathbf{e}_l$. For example, if $m \neq l$,

$$\left[J\mathcal{R}^{lm}\frac{\partial u}{\partial r_m}\right]^n_{\mathbf{i}+\frac{1}{2}\mathbf{e}_l} \approx A^{(4)}_{+l}\big(J_{\mathbf{i}}\mathcal{R}^{ll}_{\mathbf{i}}\big)\ A^{(4)}_{+r_l} D^{(4)}_{0m} u^n_{\mathbf{i}}. \tag{30}$$

The terms in the upwind expansion defined by (21) are approximated using difference operators that are defined at cell centers, $\mathbf{r}_{\mathbf{i}}$. For example, a fourth-order accurate approximation to $\partial^2_{r_l}\big(J\sqrt{\mathcal{R}^{ll}}\dot{U}\big)$ is given by

$$\frac{\partial^2}{\partial r_l^2}\left[J\sqrt{\mathcal{R}^{ll}}\,\dot{U}\right]^n_{\mathbf{i}} \approx D_{+l} D_{-l}\big(I - \frac{h_l^2}{12} D_{+l} D_{-l}\big)\big(J_{\mathbf{i}}\sqrt{\mathcal{R}^{ll}_{\mathbf{i}}}\,\dot{U}^n_{\mathbf{i}}\big), \tag{31}$$

which is the most accurate centered approximation that fits within the desired stencil.

4.3. Choosing the time-step

Following [1], the stability regions for the upwind scheme are approximated by a generalized ellipse of the form

$$\lambda_x^\sigma + \lambda_y^\sigma + \lambda_z^\sigma = \Lambda^\sigma,$$

where $\lambda_x \approx c\Delta t/\Delta x$, $\lambda_y \approx c\Delta t/\Delta y$, etc., and the stability region parameters σ and Λ are chosen to provide a good fit to the actual stability region. For a curvilinear grid, the time-step for the upwind-schemes is then chosen using the formula

$$\Delta t = C_{\text{cfl}} \min_{\text{grid-points}} \frac{\Lambda}{\left[\left(\frac{c}{\Delta x_{\mathbf{i}}}\right)^\sigma + \left(\frac{c}{\Delta y_{\mathbf{i}}}\right)^\sigma + \left(\frac{c}{\Delta z_{\mathbf{i}}}\right)^\sigma\right]^{1/\sigma}}, \tag{32}$$

where $\Delta x_{\mathbf{i}}$, $\Delta y_{\mathbf{i}}$, and $\Delta z_{\mathbf{i}}$ are approximations to the local grid spacings, and where C_{cfl} is a safety factor usually taken as 0.9. In two-dimensions the term involving $c/\Delta z_{\mathbf{i}}$ should be removed from the formula (32). The stability region parameters σ and Λ for the upwind scheme are taken as

Order	D	σ	Λ
2	2D	1.35	.605
4	2D	2.175	1.075
2	3D	1.35	.605
4	3D	2.175	.806

For comparison, the non-dissipative space-time scheme uses $\sigma = 2$ and $\Lambda = 1$ for any dimension and any order of accuracy.

5. Stability for wave equations on overlapping grids

As discussed in [2], self-adjoint discretizations of (3a)–(3c) for a single component grid can be developed to arbitrary order. These high-order accurate discretizations have a compact stencil, are dissipation free, and are provably stable on a single curvilinear grid. However, when overlapping grids are used, the perturbations introduced by the interpolation between component grids can disrupt the self-adjoint nature of the discretization over the physical domain, which can lead to numerical instabilities. For example in [21], a proof was presented which shows the presence of such unstable modes for wave equations on overlapping grids. These instabilities can be suppressed by adding artificial dissipation [2, 21], and the analysis in [21] indicated a form and scaling of a dissipation operator that would stabilize the schemes against instabilities related to overlapping grid interpolation. To be concrete, the fourth-order accurate scheme for the wave equation in one dimension with artificial dissipation[6] takes the form

$$\frac{u_i^{n+1} - 2u_i^n + u_i^{n-1}}{\Delta t^2} = c^2\big(D_+D_- - \frac{h^2}{12}(D_+D_-)^2\big)\,u_i^n - c_d\,h^4\big(D_+D_-\big)^2\big(\frac{u_i^n - u_i^{n-1}}{\Delta t}\big), \tag{33}$$

where c_d is the coefficient of the dissipation. For *weak* instabilities, c_d can be taken $\mathcal{O}(1)$ as $h \to 0$ and the scheme remains fourth-order accurate since the last term is $\mathcal{O}(h^4)$. However, for stronger instabilities, such as those that may occur with *narrow* boundary grids that keep a fixed number of points when the mesh is refined, the analysis in [21] indicates that it is necessary to take $c_d = \mathcal{O}(1/\Delta t)$, which would cause the scheme to degrade to third-order accuracy.

It was also shown in [21] that skew-symmetric (centered) discretizations of the wave equation in *first-order form* can exhibit similar unstable behavior when used with overlapping grids. However, the dissipation inherent in standard upwind-style discretizations of the first-order system was shown to have a form and scaling that would stabilize the scheme against even *strong* instabilities, such as those occurring with overlapping grids and narrow boundary grid refinement. Indeed, upwind discretizations of the first-order system

[6] The dissipation is an approximation to $c_d\,h^4\,\partial_x^4\partial_t u$.

on overlapping grids have been found to be stable and robust for wave problems including those from solid mechanics [21] and high-speed flow [32]. A similar form of dissipation has since been shown to be naturally present in "upwind" discretizations of the wave equation in second-order form, as described in [1], and the purpose of this section is to study the stability of these second-order system upwind schemes on overlapping grids.

The remainder of this section is organized as follows. In section 5.1 we present a computational experiment of computing the eigenfunctions of a disk with perfectly conducting boundaries, meshed with overlapping grids, using both the upwind scheme and the traditional centered scheme with artificial dissipation of form indicated in (33). By using a fixed number of grid points in the *narrow* boundary grid as the mesh is refined, this example demonstrates the need for a *strong* dissipation with $c_d \propto 1/\Delta t$ in (33). The accuracy of the scheme is therefore degraded to third-order. The upwind scheme, however, remains stable and maintains the expected fourth-order convergence. After discussing the overlapping grid instability in Section 5.1, we present details of a normal mode (GKS) stability analysis[7] for the first-order upwind scheme used to solve the second-order wave equation on a one-dimensional overlapping grid pictured in Fig. 7. A parameter γ is introduced into the scheme so that $\gamma = 0$ gives the centered scheme while $\gamma = 1$ gives the upwind scheme. The analysis leads to a constrained polynomial system of three equations in three complex variables. By studying the solutions to this system we illuminate why the upwind scheme is found to be so robustly stable. At present a purely analytic proof of stability is beyond our reach, and instead a careful and thorough numerical search of the parameter space is performed in Section 5.3. It is shown that, as expected, there are many unstable modes for the centered scheme with $\gamma = 0$. However, as the upwind parameter γ is increased, the number of unstable solutions decreases to zero, and for $\gamma \gtrapprox 1/4$ no unstable modes are found. Subsequent computations presented in Section 6 give further strong evidence as to the stability of the upwind schemes.

5.1. Stability and convergence for thin boundary grids

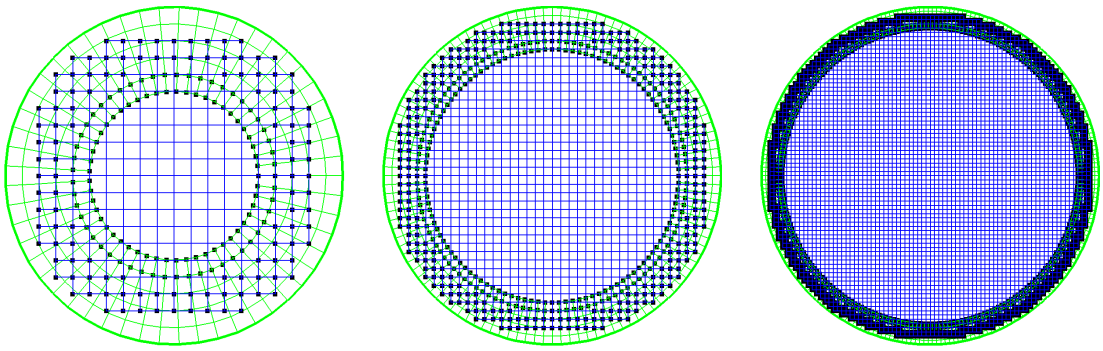

Figure 4: Three levels of grid refinement for a disk with an rectangular background grid and an thin annular boundary fitted grid. For a fixed number of radial grid points, the interpolation interface between the two grids approaches the physical boundary and an $\mathcal{O}(h^3)$ dissipation is needed to stabilize the traditional centered scheme. See Figure 5 for a plot of a typical instability arising in this case.

To illustrate the instabilities that can occur with non-dissipative schemes on typical overlapping grids, we consider computing the eigenfunctions of Maxwell's equations (TE_z mode) on a unit disk $D = \{(x, y) \mid x^2 + y^2 \leq 1\}$, with a perfectly conducting boundary. As shown in Fig. 4, a mesh for D is constructed from two component grids: a Cartesian (rectangular) background grid and an annular grid fitted to the domain boundary. Details of the composite grid are described in Appendix A. As the grid is refined, the number of radial grid points on the boundary grid remains fixed, which is a natural choice for computational efficiency since the Cartesian grid implementation can be an order of magnitude faster than curvilinear grid versions. As a consequence, as the grids are refined the boundary grid becomes narrower in physical space, and so the Cartesian grid contains an increasing fraction of the total grid points. As

[7] See, for example, [27, 28, 33] for more details of the GKS approach.

a result, the overall computational cost will approach that of a Cartesian grid. The encroachment of the interpolation boundary near to the physical boundary allows spurious waves to become trapped. This can lead to the appearance of unstable high-frequency modes in the dissipation free scheme, as shown in Fig. 5 for a two-dimensional simulation and in Fig. 11 for a one-dimensional case.

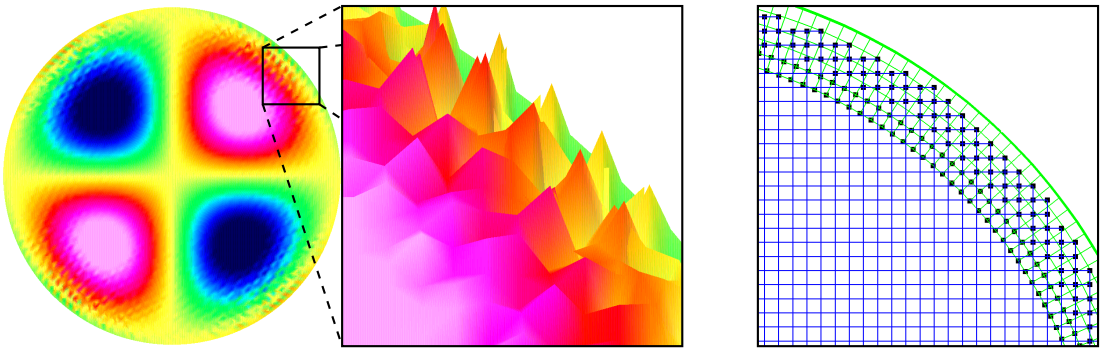

Figure 5: Example of a high-frequency unstable mode in the dissipation-free centered scheme. The instability is excited by interpolation points being located near the physical boundary. The zoomed image of the computed solution is pitched slightly away from the reader to make the surface more visible. At right is the computational grid used for this case.

To suppress the instability, dissipation is added to the fourth-order accurate centered scheme following the form given in (33) with coefficient c_d. To prevent instabilities in this difficult case of a thin boundary grid, it is necessary to scale $c_d \propto 1/h$; thus c_d is doubled when the mesh spacing is reduced by a factor of two. Using this approach, results of a grid convergence study for the traditional centered scheme with added dissipation (FD44) are given in Fig. 6. The value of c_d was determined experimentally on the coarsest grid and then doubled as the mesh spacing was halved. Also in Fig. 6 are the results of a similar convergence study using the upwind scheme (SOSUP44). To make the problem more illustrative, the number of points in the radial direction on the annular grid was taken as small as possible, $N_r = 3$ (in practical computations, the number of radial points is generally a larger value such as 9). As expected, the maximum norm errors given in the table clearly indicate that SOSUP44 is converging with fourth-order accuracy while FD44 is only converging with third order accuracy; the degradation in the convergence rate for FD44 being due to the increasing dissipation coefficient c_d which makes the dissipation term $\mathcal{O}(h^3)$.

	SOSUP44		FD44		
h_j	E_x	r	E_x	r	c_d
1/40	2.15e-01		1.31e-01		0.2
1/80	1.15e-02	18.7	2.00e-02	6.6	0.4
1/160	6.95e-04	16.5	2.58e-03	7.8	0.8
1/320	4.11e-05	16.9	3.22e-04	8.0	1.6
rate		4.12		2.9	

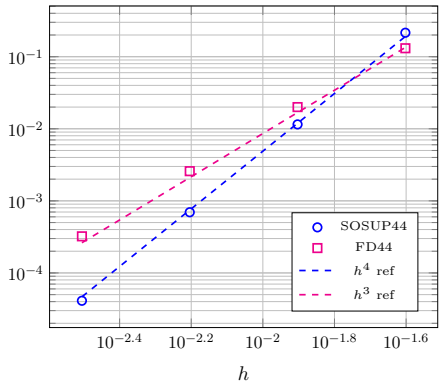

Figure 6: Convergence study for upwind (SOSUP44) and centered scheme with added dissipation (FD44) for computing the eigenmodes of a disk with think boundary grids. For each scheme and mesh resolution, the maximum error in x-component, E_x, at $t = 100$ is shown. Columns labeled r show the ratio of the errors between successive grid refinements. The final column is the coefficient c_d of the dissipation operator for FD44. The accuracy of the FD44 scheme is degraded to third-order since it is necessary to take $c_d \propto 1/h$ for stability.

5.2. Normal mode analysis for overlapping grids

To study the stability of the schemes on overlapping grids, consider a model problem consisting of the second-order wave equation $u_{tt} = u_{xx}$ for $x \in (-\infty, b)$, a Dirichlet boundary condition on the right at $x = b$, and on the left the solution is restricted to remain bounded as $x \to -\infty$. The overlapping grid used to discretize this problem is shown in Fig. 7 and consists of two grids. The grid points on the right boundary grid are given by $x_j^{(1)} = x_0^{(1)} + jh_1$, $j = 0, 1, 2, \ldots, N$, and those on the left semi-infinite grid by $x_j^{(2)} = x_0^{(2)} + jh_2$, $j = q, q-1, q-2, \ldots$. The solution approximations are denoted $u_j^{(m)}(t) \approx u(x_j^{(m)}, t)$ for $m = 1, 2$. Consider now a semi-discretization for each component grid given by,

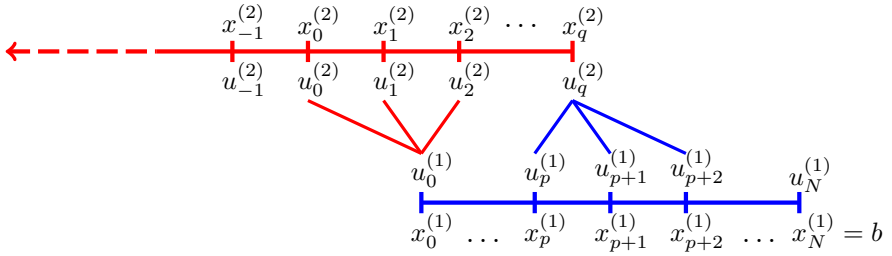

Figure 7: One-dimensional overlapping grid for the semi-infinite problem.

$$\frac{d^2 u_i^{(m)}}{dt^2} = D_+ D_- u_i^{(m)} + \gamma \frac{h_m}{2} D_+ D_- \dot{u}_i^{(m)}, \quad m = 1, 2, \tag{34}$$

where the time derivative of $u_i(t)$ is denoted $\dot{u}_i$, and we have introduced the upwinding parameter $\gamma \in [0, 1]$ as a convenient way to vary the scheme from upwind to centered. Setting $\gamma = 0$ yields the traditional second-order centered scheme with no dissipation, and $\gamma = 1$ gives the first-order upwind scheme. Boundary and interpolation conditions for the overlapping grid model problem are then given as

$$u_N^{(1)} = 0, \quad \|u^{(2)}\| < \infty, \tag{35a}$$

$$u_0^{(1)} = \sum_{k=0}^{r} a_k u_k^{(2)}, \quad u_q^{(2)} = \sum_{k=0}^{r} b_k u_{p+k}^{(2)}. \tag{35b}$$

Here a_k and b_k are interpolation coefficients for degree r polynomial interpolation from $r+1$ grid points. For quadratic ($r = 2$) interpolation for example,

$$a_0 = \frac{1}{2}(1-\alpha)(2-\alpha), \quad a_1 = \alpha(2-\alpha), \quad a_2 = \frac{1}{2}\alpha(\alpha-1), \tag{36a}$$

$$\text{where} \quad \alpha = (x_0^{(1)} - x_0^{(2)})/h_2, \quad \text{with} \quad \alpha \in [\tfrac{1}{2}(r-1), \tfrac{1}{2}(r+1)]. \tag{36b}$$

The coefficients b_k are defined similarly as

$$b_0 = \frac{1}{2}(1-\beta)(2-\beta), \quad b_1 = \beta(2-\beta), \quad b_2 = \frac{1}{2}\beta(\beta-1), \tag{36c}$$

$$\text{where} \quad \beta = (x_q^{(2)} - x_p^{(1)})/h_1, \quad \text{with} \quad \beta \in [\tfrac{1}{2}(r-1), \tfrac{1}{2}(r+1)]. \tag{36d}$$

The restrictions that α and β lie in $[\frac{1}{2}(r-1), \frac{1}{2}(r+1)]$ are a consequence of a restriction that the interpolation stencil is *centered*, i.e. the interpolation is performed from the nearest set of $r+1$ donor points.

To study stability of the discrete system we consider homogeneous initial conditions and take the Laplace transform in t, with dual variable s, to give

$$s^2 \tilde{u}_i^{(m)} = \frac{1}{h_m^2}\left(\tilde{u}_{i+1}^{(m)} - 2\tilde{u}_i^{(m)} + \tilde{u}_{i-1}^{(m)}\right) + \gamma \frac{s}{2h_m}\left(\tilde{u}_{i+1}^{(m)} - 2\tilde{u}_i^{(m)} + \tilde{u}_{i-1}^{(m)}\right), \qquad m = 1, 2, \tag{37}$$

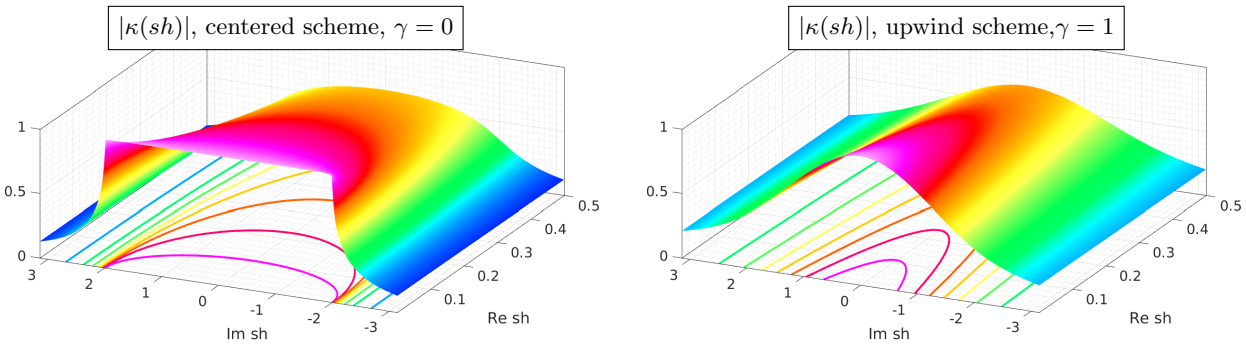

Figure 8: Surface and contour plots of $|\kappa(sh)|$ defined by equation (40) for the non-dissipative centered-scheme with $\gamma = 0$ (left) and the upwind scheme with $\gamma = 1$ (right). For $\gamma = 0$, there are branch points at $sh = \pm 2i$, while for the upwind scheme the branch cuts have been pushed into the negative $\mathrm{Re}(sh)$-plane.

with transformed boundary and interpolation conditions

$$\tilde{u}_N^{(1)} = 0, \quad \|\tilde{u}^{(2)}\| < \infty, \tag{38a}$$

$$\tilde{u}_0^{(1)} = \sum_{k=0}^{r} a_k \tilde{u}_k^{(2)}, \quad \tilde{u}_q^{(2)} = \sum_{k=0}^{r} b_k \tilde{u}_{p+k}^{(2)}. \tag{38b}$$

Here the tilde notation indicates the Laplace transformed variables. These difference equations are solved exactly by seeking solutions of the form $\tilde{u}_j^{(m)} = \kappa_m^j$. Substitution into (37) then gives the resolvent equation

$$\left(1 + \gamma \frac{z_m}{2}\right) \kappa_m^2 - \left(z_m^2 + \gamma z_m + 2\right) \kappa_m + \left(1 + \gamma \frac{z_m}{2}\right) = 0, \tag{39}$$

where $z_m = sh_m$. Writing $z_m = \xi_m + i\eta_m$, the solutions to this resolvent equation are written

$$\kappa_m = \begin{cases} \kappa_m^- & \text{for } \eta_m^2 \le \frac{\xi_m(2\xi_m^2 + 3\gamma\xi_m + 4)}{2\xi_m + \gamma}, \\ \kappa_m^+ & \text{for } \eta_m^2 > \frac{\xi_m(2\xi_m^2 + 3\gamma\xi_m + 4)}{2\xi_m + \gamma}, \end{cases} \tag{40}$$

where $\kappa_m^{\pm}$ indicates using the $\pm$ sign in the usual quadratic formula and the principle branch of the square root function is used. Note that with these definitions, $|\kappa_m| < 1$ for $\mathrm{Re}(z_m) > 0$. Fig. 8 shows surface plots of $|\kappa_m|$ for $\gamma = 0$ and $\gamma = 1$ for $\mathrm{Re}(z_m) > 0$. Note that the branch points are located at $z_m = -\gamma \pm i\sqrt{4 - \gamma^2}$, and so the branch points are on the imaginary axis for zero upwinding and in the left-half plane for $\gamma > 0$.

At this point in the analysis the standard GKS assumption is taken, i.e. that of seeking *unstable* solutions, and so $\mathrm{Re}(s) > 0$. As a result, $|\kappa_m| < 1$. Thus by enforcing the boundary conditions, $\tilde{u}_N^{(1)} = 0$, and $\|\tilde{u}^{(2)}\| < \infty$, the difference equations have solutions

$$\begin{aligned} \tilde{u}_j^{(1)} &= A(s)(\kappa_1^j - \kappa_1^{2N-j}) \quad j = 0, 1, \ldots, N-1, N \\ \tilde{u}_j^{(2)} &= B(s)\kappa_2^{q-j} \qquad\qquad\quad j = \ldots, q-1, q. \end{aligned}$$

Now applying the interpolation conditions yields a homogeneous linear system for A and B,

$$\begin{bmatrix} \kappa_1^{2N} - 1 & \sum_{k=0}^{2} a_k \kappa_2^{q-k} \\ \sum_{k=0}^{2} b_k \left(\kappa_1^{p+k} - \kappa_1^{2N-(p+k)}\right) & -1 \end{bmatrix} \begin{bmatrix} A \\ B \end{bmatrix} = \begin{bmatrix} 0 \\ 0 \end{bmatrix}. \tag{41}$$

Nontrivial solutions to (41) exist when the determinant of the matrix in (41) vanishes, which yields the determinant condition

$$G(s, \kappa_1, \kappa_2) \stackrel{\text{def}}{=} 1 - \kappa_1^{2N} - \left(\sum_{k=0}^{r} a_k \kappa_2^{r-k}\right) \left(\sum_{k=0}^{r} b_k \left(\kappa_1^k - \kappa_1^{2N-2p-k}\right)\right) \kappa_1^p \kappa_2^{q-r} = 0.$$

The stability of the discrete system is therefore encapsulated in the following theorem.

Theorem 5.1. *Discrete solutions to the one-dimensional overlapping grid problem defined by discretizations (34), boundary conditions (35a), and interpolation equations (35b) are stable (no exponential growth in time) provided there are no solutions $(s, \kappa_1(s), \kappa_2(s))$ to the system of polynomial equations*

$$G(s,\kappa_1,\kappa_2) \stackrel{\text{def}}{=} 1 - \kappa_1^{2N} - \left(\sum_{k=0}^{r} a_k \kappa_2^{r-k}\right)\left(\sum_{k=0}^{r} b_k \left(\kappa_1^k - \kappa_1^{2N-2p-k}\right)\right)\kappa_1^p \kappa_2^{q-r} = 0, \tag{42a}$$

$$P_1(s,\kappa_1) \stackrel{\text{def}}{=} \left(1+\gamma\frac{z_1}{2}\right)\kappa_1^2 - \left(z_1^2+\gamma z_1+2\right)\kappa_1 + \left(1+\gamma\frac{z_1}{2}\right) = 0, \tag{42b}$$

$$P_2(s,\kappa_1) \stackrel{\text{def}}{=} \left(1+\gamma\frac{z_2}{2}\right)\kappa_2^2 - \left(z_2^2+\gamma z_2+2\right)\kappa_2 + \left(1+\gamma\frac{z_2}{2}\right) = 0, \tag{42c}$$

that satisfy $|\kappa_m| < 1$ for $m = 1, 2$, and $\mathrm{Re}(s) > 0$, where $z_m = sh_m$.

The polynomial system (42a)-(42c), with its associated constraints, encapsulates the notion of stability for the IBVP on overlapping grids. The quadratic equations for κ_1 and κ_2 determine solutions to the Cauchy problem, and $G(s, \kappa_1, \kappa_2)$ incorporates the boundary conditions and the interpolation between grids. Since $G(s, \kappa_1, \kappa_2)$ depends on many parameters, including boundary grid points, interpolation points, and grid spacings, and since the solution to the quadratic equations for κ_m is somewhat unwieldy for nonzero γ, it is for the moment beyond our capacity to determine *a-priori* if there exist unstable solutions to (42a)-(42c). On the other hand, as shown previously in [21], for the dissipation-free case of $\gamma = 0$, one can readily find grid configurations by direct computation so that (42a)-(42c) are satisfied with $\mathrm{Re}(s) > 0$. However, a detailed and comprehensive numerical search for the upwind case with $\gamma = 1$, as discussed in Section 5.3, reveals that there appear to be no unstable solutions for the upwind scheme. We will now give some indications why this is the case without giving a formal proof, before proceeding to the discussion of the numerical search itself.

One key observation is that unstable modes will occur only when $|\kappa_m|$ are close to one and when (p, q, N), parameters indicating the relative placement of the interpolation and physical boundaries, are not too large. This observation is quantified in the following lemma.

Lemma 5.2. *There are no unstable solutions to the one-dimensional overlapping grid problem defined by discretizations (34), boundary conditions (35a), and interpolation equations (35b) when*

$$|\kappa_1|^{2N} + C_r^2(1 + |\kappa_1|^{2N-2p-r})\,|\kappa_1|^p\,|\kappa_2|^{q-r} < 1 \tag{43}$$

where

$$C_r = \max\left\{\sum_{k=0}^{r}|a_k|, \sum_{k=0}^{r}|b_k|\right\}.$$

Proof From (42a) and the triangle inequality it follows that

$$|G(s,\kappa_1,\kappa_2)| \geq 1 - \left|\kappa_1^{2N}\right| - \left|\sum_{k=0}^{r} a_k\kappa_2^{r-k}\right|\left|\sum_{k=0}^{r} b_k\left(\kappa_1^k - \kappa_1^{2N-2p-k}\right)\right||\kappa_1|^p|\kappa_2|^{q-r}.$$

Using $|\kappa_m| < 1$, $r > 0$, $p \geq 0$, $q - r \geq 0$ $N > 0$ and $2N - 2p - r \geq 0$ gives

$$\left|\sum_{k=0}^{r} a_k\kappa_2^{r-k}\right| \leq \sum_{k=0}^{r}|a_k| \leq C_r,$$

and

$$\begin{aligned}\left|\sum_{k=0}^{r} b_k\left(\kappa_1^k - \kappa_1^{2N-2p-k}\right)\right| &\leq \left|\sum_{k=0}^{r} b_k\kappa_1^k\right| + \left|\sum_{k=0}^{r} b_k\kappa_1^{2N-2p-k}\right| \leq \left|\sum_{k=0}^{r} b_k\right| + \left|\sum_{k=0}^{r} b_k\right||\kappa_1|^{2N-2p-r} \\ &\leq C_r(1+|\kappa_1|^{2N-2p-r})\end{aligned}$$

Thus $|G(s, \kappa_1, \kappa_2)| > 0$ when

$$|\kappa_1|^{2N} + C_r^2(1 + |\kappa_1|^{2N-2p-r})\,|\kappa_1|^p\,|\kappa_2|^{q-r} < 1,$$

and this completes the proof.

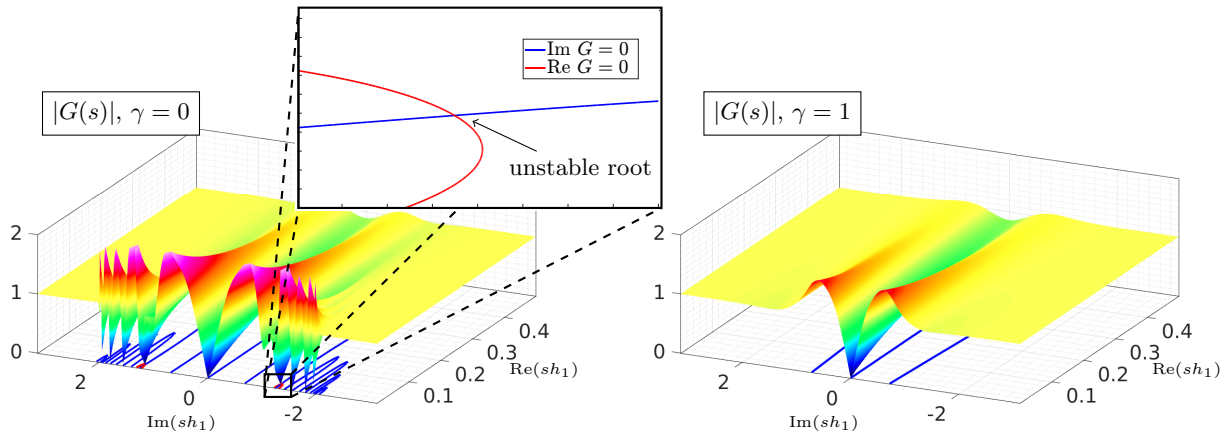

Figure 9: Absolute value of the determinant condition $|G(s)|$ for $\gamma = 0$ and $\gamma = 1$ on the left and right respectively. Beneath the surface plots are contours of the real and imaginary parts in red and blue. Intersections of these contours of indicate an unstable mode, which occur here at $sh_1 \approx 0.01747 - 1.251i$.

Note that under our assumptions for valid interpolation formulae, for $r = 1$ (linear interpolation) $C_r \leq 1$ while for $r = 2$, $C_r \leq 5/4$. Thus from (43) it follows that for given (p, q, N) there will be no unstable roots for κ_m small enough. For example if $|\kappa_m| < \delta < 1$ then there will be no unstable roots when

$$\delta^{2N} + C_r^2(1 + \delta^{2N-2p-r})\delta^{p+q-r} < 1. \tag{44}$$

For example consider the case $N = 10$, $p = 1$, $q = 4$, and $r = 3$, for which condition (44) implies there are no unstable modes when $|\kappa_m| < \delta \approx 0.8$. The surface plots of $|\kappa_m|$ in Fig. 8 shows that for the dissipation-free case $|\kappa_m|$ is close to one for $\mathrm{Re}(sh_m)$ small and $\mathrm{Im}(sh_m)$ between approximately -2 and 2. On the other hand, for the upwind scheme $|\kappa_m|$ is only close to 1 when both $\mathrm{Re}(sh_m)$ and $\mathrm{Im}(sh_m)$ are small. In addition, for small sh_m the discrete solutions is an accurate approximation to the continuous solutions and thus unstable modes in this region are unlikely. Therefore, the damping added by the upwind scheme has reduced the possibility for unstable modes, and in particular has decreased the likelihood of unstable high-frequency spatial modes quite dramatically. High-frequency modes that are not well represented on the grid are typical of the unstable modes observed in overlapping grid computation.

Fig. 9 illustrates these observations by showing $|G(sh_1)|$ for an overlapping grid configuration yielding instability for the centered scheme with $\mathrm{Im}(sh_1) \approx 1.5$, while the same grid configuration for the upwind scheme has no unstable roots[8]. In addition, notice that the location of the unstable mode in the sh_1-plane indicates that this mode is highly oscillatory on the grid, consistent with the observed unstable modes in two dimensions in Fig. 5 and in one-dimension in Fig. 11. The surface plot of $|G(sh_1)|$ for the non-dissipative scheme shows an oscillatory behavior near the imaginary axis where the surface almost reaches zero at a number of points; these are points where there is almost an unstable high-frequency mode. By contrast the surface plot of $|G(sh_1)|$ for the upwind scheme is smooth and close to one in the same regions indicating there are no nearby unstable roots at high frequencies. The only place where $|G(sh_1)|$ is close to zero for the upwind scheme is near the origin, $s = 0$, but this expected behavior for consistent schemes.

To further understand the role of dissipation, it is instructive to consider the spectra of the spatial discretization operator for the dissipation-free and upwind cases. In order to facilitate this, the semi-infinite domain is truncated at a finite but suitable large size using $x \in (x_0^{(2)} - Mh_2, x_0^{(1)} + Nh_1)$, for some large integer M, and Dirichlet conditions are applied at both the left and right ends. Such a procedure was also used in [21] which showed the discrete spectra for finite domains converges to the spectra for the semi-infinite domain as M increases. This finite domain wave equation is now approximated using second-order centered ($\gamma = 0$) or first-order upwind ($\gamma = 1$) using either a single grid, or an overlapping grid with near boundary geometry similar to that shown in Fig. 7. The eigenvalue decomposition for the resulting discretization

[8]Note that the factor h_1 has been included as a measure of grid spacing to scale the dual variable s for convenience, but h_2 could have been chosen as well.

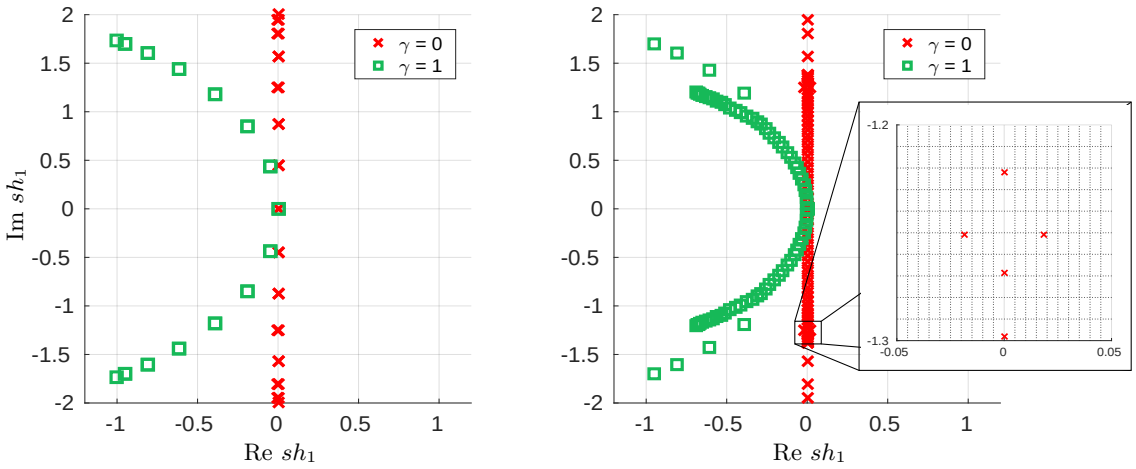

Figure 10: Location of the eigenvalues, in the complex sh-plane, of the discretization matrix for a Dirichlet problem on a large finite domain. On the left is the result for a single grid, and on the right for an overlapping grid with a near-boundary grid as shown in Fig. 7. For the first-order accurate upwind scheme with $\gamma = 1$ the roots lie along the curve in the left-half plane, and all modes except the one at $sh_1 = 0$ decay in time. For the dissipation-free scheme there are two unstable modes with $\mathrm{Re}(sh_1) > 0$ which are complex conjugates. The unstable mode detailed in the inset figure at right is is an approximation to the unstable mode in Fig. 9. Note that the number of roots differ on the left and right since an adequate number of points is needed to observe the unstable mode.

matrices are then computed, and the location of the eigenvalues in the complex plane are plotted in Fig. 10[9]. For the non-dissipative scheme ($\gamma = 0$) on a single grid, the roots in the sh plane lie on the imaginary axis on the interval $I = \{\, i\xi \mid \xi \in [-2, 2]\}$, where $\xi = \mathrm{Im}(sh)$ and $\eta = \mathrm{Re}(sh)$. These roots have $\mathrm{Re}(sh) = 0$ and thus correspond to oscillatory modes in time that neither grow nor decay. For the upwind scheme ($\gamma = 1$), all roots except the root $\kappa = 1$ at $sh = 0$ are shifted onto a curve in the left half plane. These roots in the left-half sh plane correspond to modes that decay in time, and modes with higher spatial frequency (increasing $\mathrm{Im}(sh)$) have increased temporal damping. For the case of the overlapping grid, the inter-grid interpolation introduces perturbations to the location of the eigenvalues of the discretization matrix. Given the spectra for the single grid case, it is obvious that such small perturbations could easily push the dissipation-free scheme into instability, while it is less likely that the upwind scheme would become unstable for similar sized perturbations because the eigenvalues have large negative real part. This supposition is indeed born out in the spectra for the overlapping grid case in Fig. 10 which shows that for the non-dissipative case an instability is induced, while the upwind scheme remains stable. The example we have just described has been chosen closely correspond to the unstable root shown in Fig. 9, with the lone difference being the large finite domain approximation of the semi-infinite domain discussed in Fig. 9. To illustrate the closeness of the two results, Fig. 11 shows the real part of the spatial eigenfunction for the two cases, the semi-infinite grid and the truncated approximation. Clearly the two modes are indeed very similar. In addition, both eigenfunctions illustrate the oscillatory nature of the unstable modes for dissipation-free schemes on overlapping grids.

5.3. Grid parameter space search for unstable modes

Because a closed-form proof of stability is, at present, intractable, a careful numerical search is instead performed for a range of valid overlapping grids. We therefore seek unstable roots (s, κ_1, κ_2) to the constrained polynomial system (42a)-(42c). For a given overlapping grid configuration (e.g. the grid overlap, ratio of grid spacings and order of interpolation), the polynomial system (42a)-(42c) is completely specified, and the roots may be computed. In particular, this work uses the Gröbner Basis method [34], and homotopy

[9]Note that there appear to be two sets of modes on the overlapping grid case for both $\gamma = 0$ and $\gamma = 1$. This is due to the axes being scaled by h_1 so that modes corresponding to the near-boundary grid match the modes in the left plot while modes corresponding to the large domain grid seem out of place. The choice is arbitrary and if the axes were scaled by h_2, the situation would be the opposite.

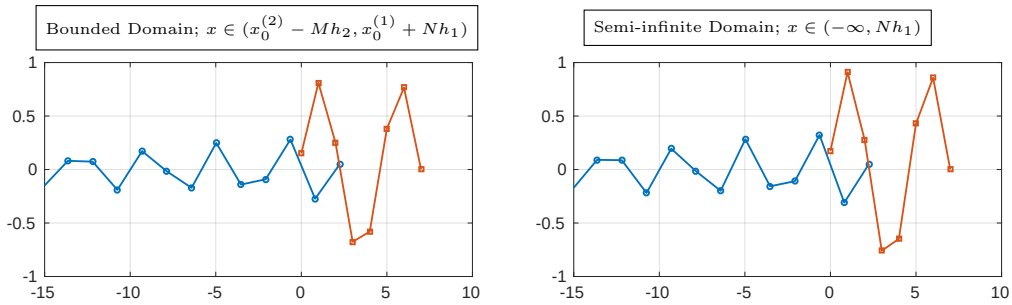

Figure 11: Real part of an eigenfunction corresponding to an unstable mode for the truncated domain and semi-infinite domain on the left and right respectively. The corresponding unstable mode is the same mode pictured in Figures 9 and 10. It's clear that the truncated domain problem gives good agreement to results obstained for the semi-infinite problem. For the approximation shown here, the bounded domain is approximately $x \in (-300, 7)$.

continuation [35]. The Gröbner Basis method is guaranteed to find all roots of the polynomial system, but we have found it to be somewhat expensive. On the other hand, homotopy continuation is quite fast, but is not guaranteed to find all roots (although we have yet to encounter a case where roots were missed). We therefore use the homotopy continuation for the majority of the results presented, and rely on the Gröbner Basis method as a check of the completeness of the results.

Solutions to the *unconstrained* polynomial system (42a)-(42c) are computed using the polynomial system solver PHCpack [36], which uses a homotopy continuation method as discussed in [35]. This resulting roots may contain some that do not satisfy $|\kappa_m| < 1$ and $\mathrm{Re}(s) > 0$, as required in Theorem 5.1, and so these invalid roots are eliminated from further consideration. Any remaining roots would represent instability of the overlapping grid discretization on the semi-infinite domain with thin boundary fitted grid. Note however, that these roots are nearly identical to nearby unstable roots found for a large finite domain after appropriate reformulation of the discretization in equations (34)–(35). The eigenvalues of the finite-dimensional discretization matrix are easily computed, and any unstable roots, i.e. those with $\mathrm{Re}(s) > 0$, can be compared to the unstable roots for the semi-infinite domain from the constrained polynomial system. Any unstable roots for the finite domain problem are found to converged to the unstable roots for the semi-finite domain as the length of the finite domain became larger. This check is a further confirmation that the unstable solutions obtained via the polynomial system do indeed correspond to instability in the original semi-discrete equations (34)–(35).

A numerical search for unstable solutions as discussed in Theorem 5.1 is now performed. The space of valid grid configurations as shown in Fig. 7, as well as the upwind parameter γ, is discretized and all unstable roots are reported. A full list of input data to the generic parameter space search is given in the table below

Parameters for Search Algorithm	
γ	: upwind parameter, $\gamma \in [0, 1]$
r	: Order of interpolation (e.g. 1 or 2)
N	: Number of grid cells on thin grid (e.g. 5)
h_1	: Grid spacing on thin boundary grid
$\delta \stackrel{\text{def}}{=} \frac{h_2}{h_1} = \delta_{\min} + j\Delta\delta,\ j = 0, \ldots, M_\delta,$	: Grid spacing ratio
M_δ	: number of intervals to use in the δ search space
$[\delta_{\min}, \delta_{\max}]$	: minium and maximum grid spacing ratio
$x_0^{(1)} = 0$	: Left point of thin grid,
M_x	: number of intervals to use in the $x_0^{(2)}$ search space
$x_0^{(2)} = -\frac{r+1}{2} + j\Delta x_2,\ j = 0, \ldots, M_x,$	: Left donor point on semi-infinite grid,
$x_p^{(1)} = ph_1,\ p = 1, 2, \ldots N - r$	: Left donor point of thin grid,
$x_q^{(1)} = x_0^{(2)} + qh_2,\ q = q_{min}, \ldots, q_{max}$	: Interpolation point on semi-infinite grid

where

$$\Delta\delta \stackrel{\text{def}}{=} \frac{\delta_{\max} - \delta_{\min}}{M_\delta}, \quad \Delta x_2 = \frac{x_{0,max}^{(2)} - x_{0,min}^{(2)}}{M_x}. \tag{45}$$

However, a number of these parameters are not independent and the search space can be reduced in size somewhat. In particular, without loss of generality the grid spacing on the boundary grid can be normalized so that $h_1 = 1$, and the left end of the thin boundary grid can be fixed at $x_0^{(1)} = 0$. Also note that p in the formula $x_p^{(1)} = ph_1$ is limited between 1 and $N - r$ since there must be enough donor points for interpolation. Thus for a given ratio δ, bounds on $x_0^{(2)}$ and q can be determined by substituting $x_q^{(2)} = x_0^{(2)} + qh_2$ and $x_p^{(1)} = x_0^{(1)} + ph_1$ into the interpolation formula (36d) for β and enforcing the condition that the interpolation is centered so that α and $\beta \in \left[\frac{1}{2}(r-1), \frac{1}{2}(r+1)\right]$. For practical computation, the two grids should not be of dramatically different resolutions, and so the ratio of the grid spacings, δ, can be restricted to a reasonable interval around 1, here $\delta \in [1/4, 4]$. Also since the case of $\gamma = 0$ is the standard second-order accurate centered discretization of the wave equation, we take the interpolation order to be $r = 2$ as required for second-order accuracy. Finally, because the primary interest is in the thin boundary grid case, we present results for a boundary grid with $N = 5$ points which is much smaller than typically used in practice. The parameter space is therefore defined by the following choices

r	$x_0^{(1)}$	h_1	N	$\delta_{\min}$	$\delta_{\max}$	M_x	M_δ
2	0	1	5	1/4	4	40	40

for which results are now presented.

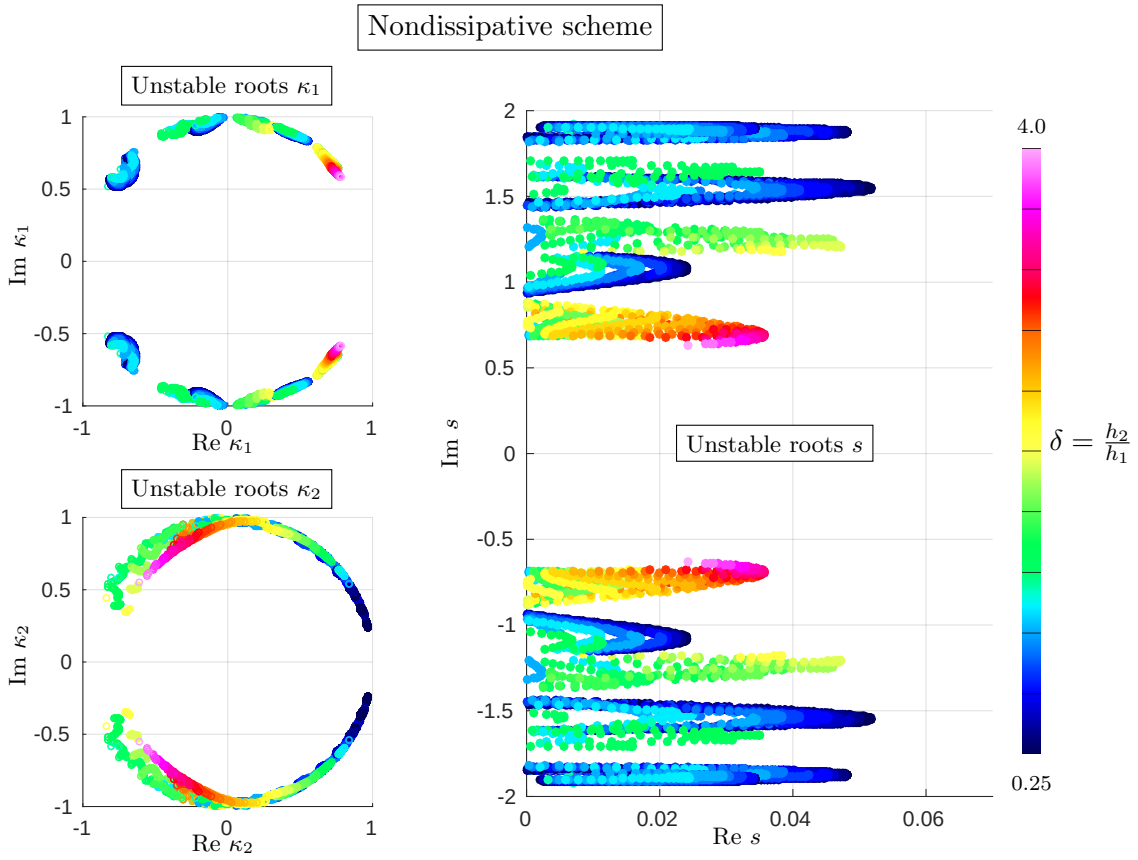

Figure 12: Scatter plots of the computed unstable roots (s, κ_1, κ_2) for the nondissipative scheme ($\gamma = 0$) for $N = 5$ points on the thin boundary grid. Left: Values of κ_1 and κ_2 (unstable roots have $|\kappa_m| < 1$). Right: Values of s (unstable roots have $\mathrm{Re}(s) > 0$). The coloring indicates the ratio of grid spacings $\delta = h_2/h_1$.

Fig. 12 shows all the unstable roots (s, κ_1, κ_2) for the non-dissipative scheme with $\gamma = 0$. The plots on on the left side of Fig. 12 show $\kappa_1^{(i)}$ and $\kappa_2^{(i)}$, while the plot on the right shows $s^{(i)}$ where $i = 1, 2, \ldots, N_s$ denotes the different unstable roots. The colors in the figure correspond to the ratio of the grid spacings for that particular root. Recall that the growth rate in time of a particular unstable modes is given by $e^{\mathrm{Re}(s)t}$.

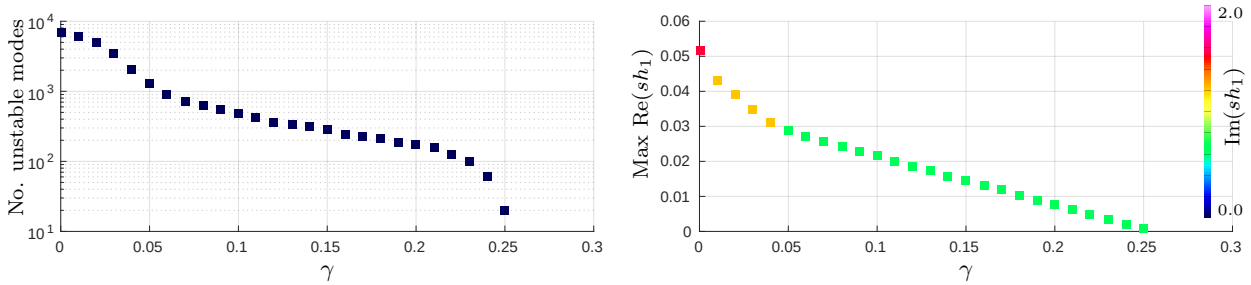

Figure 13: At left is a semi-log plot of the number of unstable modes found in the parameter space search versus the value for the upwinding parameter γ. At right is the maximum growth rate given by $\mathrm{Re}(s)$ taken over all unstable modes for a given value of γ, where the points are colored by the magnitude of $\mathrm{Im}(s)$.

Therefore if there is an an unstable mode with $\mathrm{Re}(sh_1) = \sigma_0 > 0$, then the growth rate in time is $e^{(\sigma_0/h_1)t}$ and the growth becomes unbounded as the mesh is refined and $h_1 \to 0$. For $\gamma = 0$, many thousands of unstable roots were found in the parameter space considered. From the plot of $s^{(i)}h_1$ it is seen that the most unstable roots, i.e. those with larger values of $\mathrm{Re}(s^{(i)}h_1)$, tend to appear in bands near where the grid ratio δ is either an integer or the inverse of an integer. It can also be seen that there are no unstable roots for well resolved solutions when sh_1 is small. In particular there are no unstable roots for $|sh_1| < C_s \approx \pi/5 \approx 0.628$. Thus, only those modes with a high frequency with respect to the grid spacing appear to be unstable. For those high frequency modes the dissipation in the upwind scheme is found to have the most significant stabilizing effect as discussed previously in Section 5.2.

To understand how the upwinding parameter γ affects the stability, we conduct a series of parameter space searches for different values of γ between zero and one,

$$\gamma = \frac{j}{100}, \quad j = 0, 1, ..., 100.$$

Fig. 13 shows both the number of unstable modes versus γ, as well as the largest growth rate for the unstable modes versus γ. Both quantities are monotonically decreasing with respect to the upwinding parameter, and there are no unstable modes for $\gamma \gtrapprox .25$. The plot on the right of Fig. 13 also uses color to encode the size of $\eta \stackrel{\text{def}}{=} \mathrm{Im}(sh_1)$ for the roots with largest growth factor. The value of η indicates how rapidly the eigenmode oscillates in both time and space. For small γ the most unstable roots correspond to a high frequency of $\eta \approx 1.5$. However, the upwind scheme introduces the most dissipation for high-frequencies and as γ increases these modes become stabilized which reveals lower values of η. By $\gamma \approx .25$ the most unstable mode has $\eta \approx 0.7$, still a moderately high frequency the grid. For $\gamma \gtrapprox .25$ no unstable modes are found, giving strong evidence that the first-order upwind scheme is indeed stable for $\gamma = 1$. Furthermore, in practical two-dimensional and three-dimension simulations of the wave equation and Maxwell's equations we have never observed any numerical instabilities with the upwind scheme.

6. Numerical Results

In this section, numerical results are presented to verify the implementation, numerical convergence, and stability of the upwind scheme for Maxwell's equations in second-order form on overlapping grids. A variety of different configurations are considered, and grid refinement studies are performed to assess the accuracy of the solution as the mesh is refined. Problems are selected to demonstrate both the properties of the numerical scheme, as well as how overlapping grids can be used to accommodate curvilinear geometries and varying material parameters. The first problem considered is the scattering of an electromagnetic plane wave from a perfectly conducting cylinder in two dimensions in order to demonstrate the accuracy and stability of the upwind scheme for a simple two-dimensional geometry. The next problem deals with scattering of a plane wave from a dielectric cylinder and is used to evaluate the scheme for a problem with material interfaces. Analogous problems of scattering from perfectly conducting and dielectric spheres are then used to demonstrate the extension to three space dimensions. The first four problems are classical scattering and

all have known exact solutions [37–39] which permits the errors to be determined. A final, more complicated example, considers a *chirped frequency* plane wave impinging on a rectangular-shaped conducting body embedded in a dielectric slab. In this case, where the exact solution is not known, Richardson extrapolation is used to estimate the errors and convergence rates. In all cases, detailed descriptions of the composite grids used in the computations are presented in Appendix A. All numerical studies are performed with the Overture[10] based CgMx solver. Overture provides tools to generate high quality composite grids for high-order methods along with a suite of PDE solvers for various problems in computational physics (compressible and incompressible flows, solid mechanics, conjugate heat transfer, electrodynamics, etc). Overture's overlapping structured grid generator Ogen is used to create all of the composite grids and the CgMx solver is used to compute all the solutions.

6.1. Scattering from a perfectly conducting cylinder

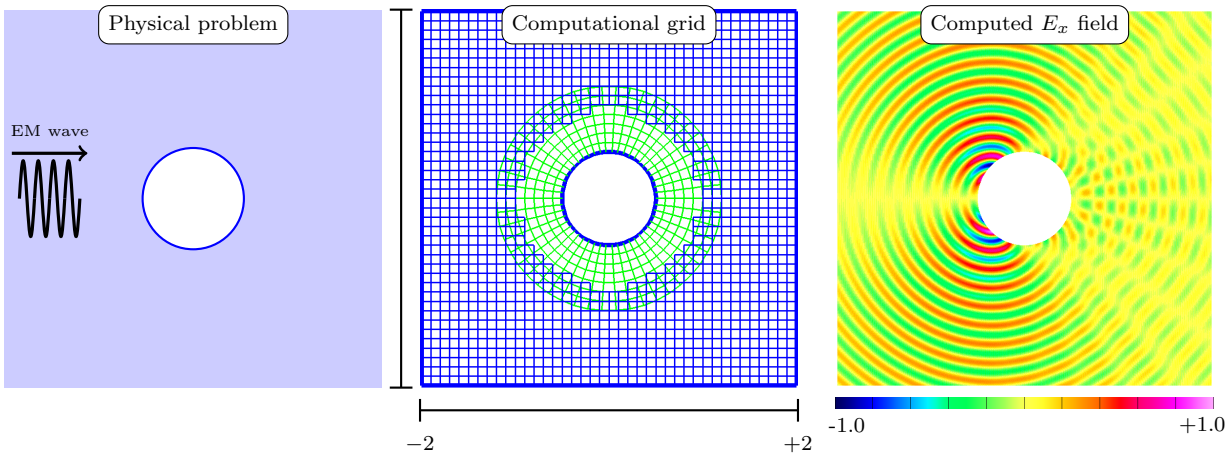

Figure 14: Left: Diagram illustrating the physical setup for the scattering of a TE_z plane-wave incident on a conducting cylinder. Middle: Overlapping grid for the domain (coarse grid). Right: Computed solution showing E_x at $t = 1$ (on a fine grid with $h \approx \frac{1}{160}$) for an incident wave-number $k_x = 5$.

Consider the classical problem of scattering of a uniform electromagnetic plane wave propagating in the positive x-direction impinging normally on a perfectly conducting cylinder of a given radius R. Such a problem is illustrated in Fig. 14, which also shows a representative computational grid, and a computed scattered field as discussed below. The incident wave is polarized as a TE_z mode (i.e. with non-zero components E_x, E_y and H_z) and propagates in the positive $x-$direction,

$$E_x^I = 0, \quad E_y^I = -Z\, e^{i(k_x(x-ct))}, \quad H_z^I = e^{i(k_x(x-ct))}, \tag{46}$$

where $Z = \sqrt{\mu/\epsilon}$ is the electrical impedance, and k_x is a given wave number. The exact solution to this classical problem is presented in many texts, for example [37–39], and the reader is referred to those works for a description of the exact solution and its derivation.

For the computations presented here, the infinite space is truncated to the square $[-2, 2] \times [-2, 2]$, and the radius of the cylinder is taken to be $R = 0.5$. The resulting two-dimensional domain is meshed with two component grids, a green boundary fitted grid near the cylinder and a blue background Cartesian grid, as shown in Fig. 14. This composite grid is described in more detail in Appendix A.2. The annular grid has a perfectly conducting boundary condition (1b) on the inner radius while the background rectangular grid has outer boundary conditions set using the known exact solution. The initial data is also given by the known solution. The second- and fourth-order accurate upwind schemes described in Section 4 are used to compute approximate solutions with $\epsilon = 1$, $\mu = 1$, $k_x = 5$ and $c = 1$, and the results are then compared to the exact solution.

[10] http://www.overtureframework.org/

2nd Order Max-norm Convergence												
h_j	E_x	r	E_y	r	H_z	r	$\partial_t E_x$	r	$\partial_t E_y$	r	$\partial_t H_z$	r
1/40	5.7e-1		1.3e0		1.3e0		17.6e0		49.4e0		49.8e0	
1/80	1.7e-1	3.3	6.9e-1	1.9	6.9e-1	1.9	5.7e0	3.1	15.3e0	3.2	15.5e0	3.2
1/160	4.9e-2	3.6	2.1e-1	3.2	2.2e-1	3.2	1.5e0	3.7	3.9e0	3.9	4.0e0	3.9
1/320	1.3e-2	3.9	5.5e-2	3.9	5.5e-2	3.9	4.0e-1	3.8	9.7e-1	4.0	9.8e-1	4.0
rate		1.83		1.54		1.55		1.83		1.90		1.89
4th Order Max-norm Convergence												
h_j	E_x	r	E_y	r	H_z	r	$\partial_t E_x$	r	$\partial_t E_y$	r	$\partial_t H_z$	r
1/40	2.4e-1		7.7e-1		7.8e-1		7.3e0		20.8e0		21.0e0	
1/80	2.4e-2	10.1	1.0e-1	7.5	1.0e-1	7.5	6.7e-1	10.8	1.9e0	11.2	1.9e0	11.1
1/160	1.7e-3	14.0	7.4e-3	13.9	7.5e-3	13.9	5.0e-2	13.4	1.3e-1	14.2	1.3e-1	14.2
1/320	1.1e-4	15.4	4.8e-4	15.4	4.8e-4	15.4	3.5e-3	14.5	8.6e-3	15.3	8.7e-3	15.3
rate		3.71		3.57		3.57		3.69		3.76		3.75

Table 1: Max-norm error convergence study computing the scattered field from a conducting cylinder at $t = .25$ using the second-order and fourth-order accurate upwind schemes. The left-most column is the target grid spacing h_j. Columns labeled by field components contain the computed errors, and columns labeled r denote the ratio of errors for successive refinements. The two rows labeled *rate* show the computed average rate of convergence.

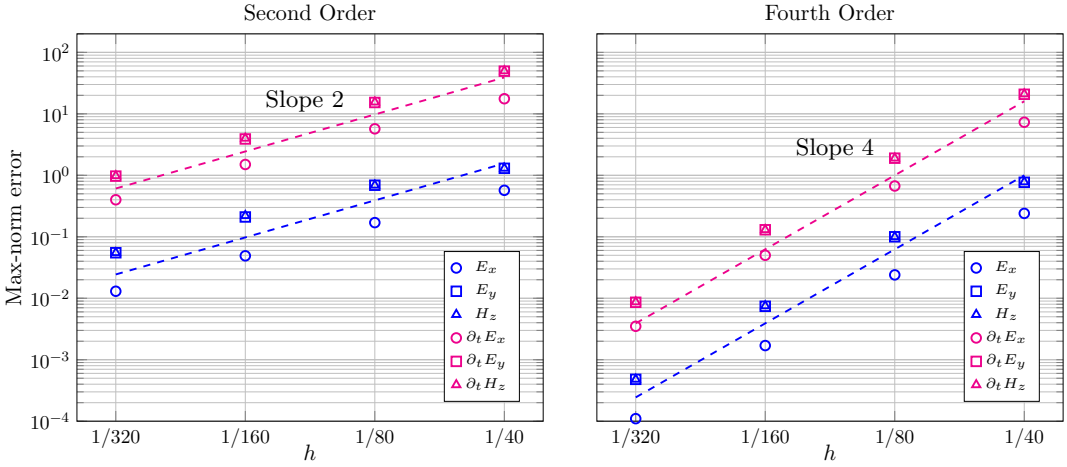

Figure 15: Max-norm error convergence plots for the second-order and fourth-order accurate upwind schemes applied to the computation of the scattered field from a conducting cylinder. The corresponding data is presented in Table 1. Dashed lines are drawn for reference showing the expected convergence rate.

Table 1 shows the maximum-norm errors for numerical convergence studies of the second- and fourth-order accurate upwind schemes for the problem of scattering from a PEC cylinder. The convergence rate is computed by a least squares fit to the log of the errors. The data shows that for both schemes the ratio of errors from one grid to the previous coarser grid are near to the expected values of 4 and 16 for the second- and fourth-order accurate schemes respectively, and the convergence rates are in excellent agreement with the theoretical prediction. The same data is depicted graphically using a log-log plot in Fig. 6.1, and again the expected convergence rates are clearly demonstrated. Note that for the given value of $k_x = 5$, the time derivatives are large compared to the field values, but the convergence rates still verify the expected theoretical value. A separate indication of the quality of the computed solution is the smoothness of the error near both the physical and the interpolation boundaries. To that end, Fig. 16 shows a computed solution for E_x, its error, and a zoomed wire frame plot of the error near the interpolation boundary at $t = 1$. Note that the error is smooth throughout the domain, and in particular the error is smooth across the interpolation interface. This can be clearly seen in the rightmost panel of the figure, where the error is

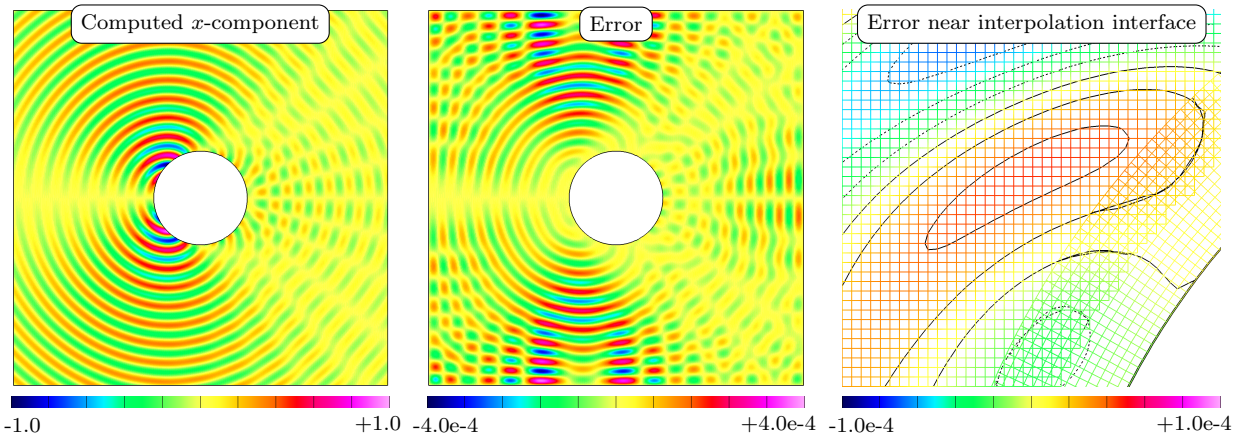

Figure 16: Left: Computed solution component E_x at $t = 1$ for $k_x = 5$ using a grid with $h \approx \frac{1}{160}$. Middle: Error in computed solution on the same grid. Note the smoothness of the numerical error which shows the effect of dissipation in the upwind scheme. Right: Zoomed wireframe plot of the error near the surface of the interpolation boundary. Black contours are drawn for each component grid and are a further indication of the smoothness of the error, even near the interpolation boundary.

plotted as a wireframe and black contour lines are included. Note that the contour lines are independently plotted on each component grid and will line up in the overlap region only if the errors agree sufficiently well. Such contour lines are thus a sensitive indicator of the smoothness of the quantity being plotted, in this case the error, and this shows the strong smoothing effect of the upwind dissipation near interpolation boundaries. The other field components are qualitatively similar and so are not plotted.

6.2. Scattering from a dielectric cylinder

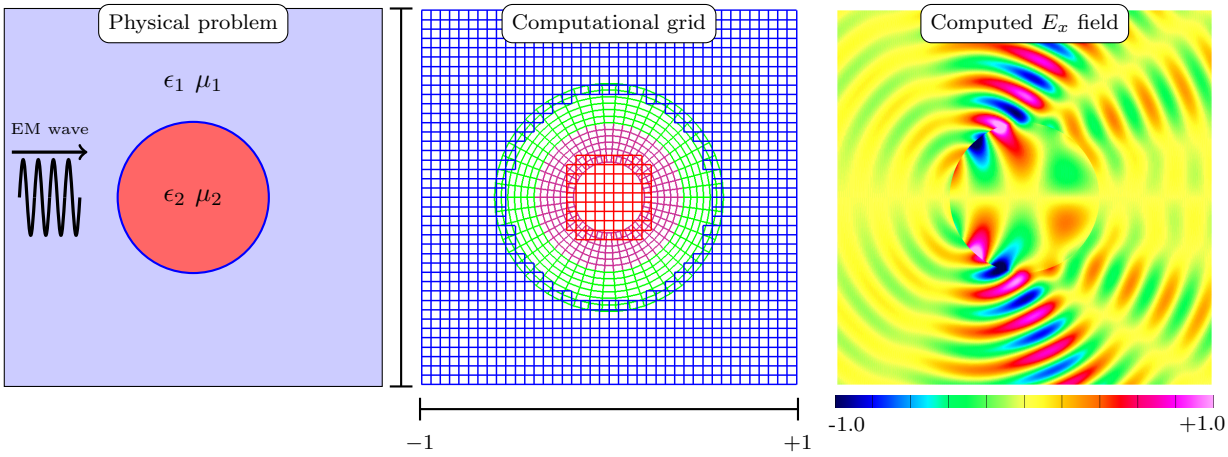

Figure 17: Left: Illustration of the physical problem of a polarized uniform plane wave scattering from a dielectric cylinder radius R in an infinite domain. Middle: A coarse overlapping grid construction for scattering from a dielectric cylinder. Right: Computed field component E_x on a fine grid with $h \approx \frac{1}{160}$ at time $t = 0.25$.

Having illustrated the performance of the upwind schemes for electromagnetic wave propagation in a single material where the geometry is treated using composite overlapping grids, we move on to the case of multiple dielectric materials. The physical scenario is similar that described in Section 6.1, but where now the interior of the cylinder is filled with a separate dielectric material, as illustrated in Figure 17. This is again a classical scattering problem, and the exact solution can be found in many texts, for example [37–39].

For the numerical results presented here, the cylinder is taken to have radius $R = .4$, and the permittivity and permeability are taken as $\epsilon_1 = 0.25$ and $\mu_1 = 1$ for the exterior domain and $\epsilon_2 = 1$ and $\mu_2 = 1$ for the interior region. The physical domain is truncated to the square $[-1, 1] \times [-1, 1]$. The computations presented

2nd Order Max-norm Convergence

h_j	E_x	r	E_y	r	H_z	r	$\partial_t E_x$	r	$\partial_t E_y$	r	$\partial_t H_z$	r
1/40	3.2e-1		6.1e-1		6.3e-1		9.7e0		1.7e1		1.8e1	
1/80	8.9e-2	3.6	1.7e-1	3.5	1.8e-1	3.6	3.0e0	3.2	3.6e0	4.8	4.2e0	4.2
1/160	2.1e-2	4.2	4.3e-2	4.0	4.5e-2	4.0	7.8e-1	3.9	8.2e-1	4.4	1.1e0	4.0
1/320	4.9e-3	4.3	1.1e-2	4.1	1.1e-2	4.0	2.2e-1	3.6	2.1e-1	4.0	2.7e-1	4.0
rate		2.01		1.95		1.95		1.84		2.13		2.01

4th Order Max-norm Convergence

h_j	E_x	r	E_y	r	H_z	r	$\partial_t E_x$	r	$\partial_t E_y$	r	$\partial_t H_z$	r
1/40	2.4e-2		1.1e-1		1.2e-1		7.7e-1		3.6e0		3.8e0	
1/80	1.9e-3	12.5	5.2e-3	21.2	5.4e-3	22.2	5.9e-2	13.1	1.1e-1	34.2	1.2e-1	30.6
1/160	1.3e-4	14.6	3.5e-4	15.1	3.5e-4	15.2	3.9e-3	14.9	6.6e-3	16.0	8.4e-3	14.9
1/320	9.6e-6	13.6	2.2e-5	15.7	2.3e-5	15.7	3.0e-4	13.2	4.5e-4	14.5	5.4e-4	15.5
rate		3.77		4.08		4.10		3.79		4.29		4.23

Table 2: Max-norm error convergence study for the scattered field from a dielectric cylinder using the second-order and fourth-order accurate upwind schemes. The left-most column is the target grid spacing h_j, columns labeled by field components contain errors at $t = .25$, and columns labeled r denote the ratio of errors for successive refinements. The two rows labeled *rate* show the computed average rate of convergence. Excellent agreement with the theoretical convergence rates is observed.

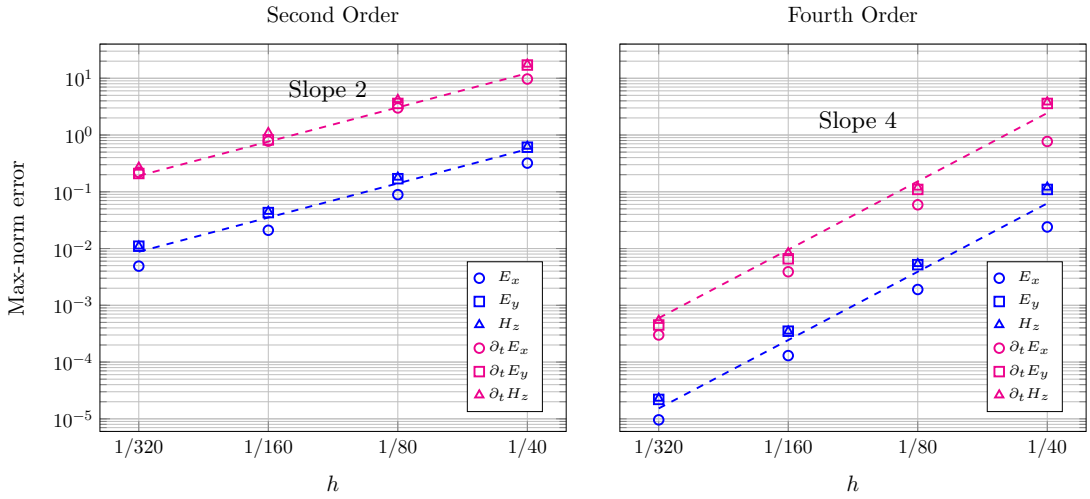

Figure 18: Max-norm error convergence plots for the second-order and fourth-order accurate upwind schemes applied to the computation of the the scattered field from a dielectric cylinder. Dashed lines are drawn for reference showing the expected convergence rates. These results correspond to those in Table 2, and demonstrate excellent agreement with the expected convergence rates.

here describe the physical system using two composite grids, one for the interior material and one for the exterior materials, and each of these is composed of two component grids. In the center panel of Figure 17, the exterior composite grid has a green boundary fitted grid and a blue background Cartesian grid, while the interior material has a maroon boundary fitted grid and a red Cartesian background. See Appendix A.3 for additional details of the two composite grids. The incident plane wave is again given by (46) with $k_x = 5$, and the initial state of the field is given by the known time-harmonic solution which is also used for the numerical boundary data for the artificially truncated exterior. Figure 17 shows a representative computed solution component E_x at time $t = 0.25$. Note that the fields may jump at the material interface.

A convergence study for the problem of scattering from a dielectric cylinder is performed using both the second- and fourth-order accurate upwind schemes. Table 2 and Figure 6.2 show the result of this study where the max-norm errors in the solution components and time derivatives are shown to converge at close

to the expected rates. The fact that high-order accuracy in the max-norm is demonstrated, despite the fact that the fields may jump across the material interface, is due to the use of interface fitted grids which represent the geometry exactly, and the use of the compatibility interface conditions. See [2] for additional details of the numerical treatment of such interfaces.

6.3. Scattering from a perfectly conducting sphere

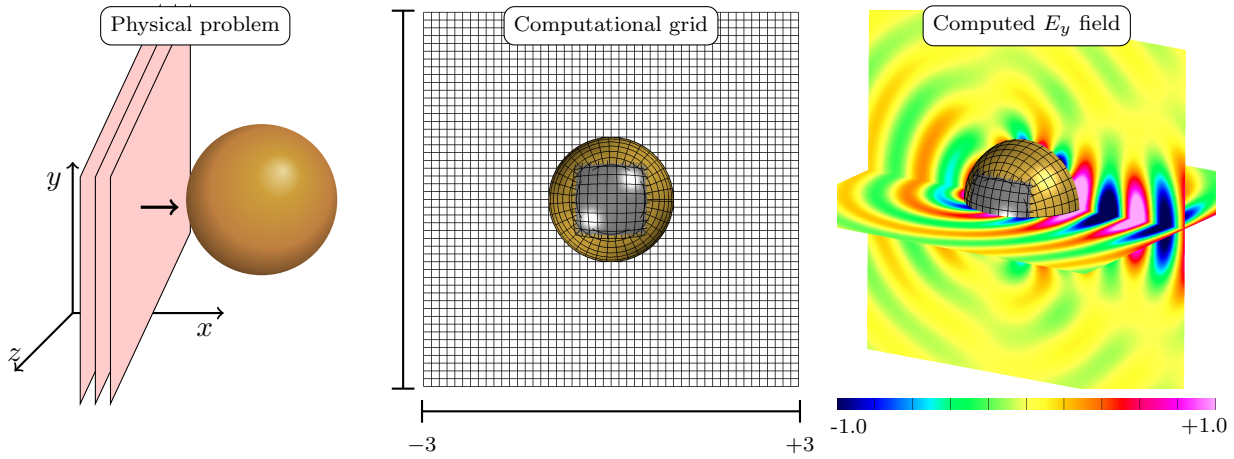

Figure 19: Left: Illustration of physical problem showing planes of constant phase impinging on the conducting sphere in an infinite domain. Middle: A coarse version of the overlapping grid for the sphere in a truncated domain. Right: Computed solution E_y with $k_x = 1$ using a mesh with grid spacing approximately equal to $h \approx \frac{1}{40}$. The overlapping grid on the sphere surface is coarsened for easier viewing.

The examples considered in Sections 6.1 and 6.2 illustrate the performance of the upwind schemes for electromagnetic wave propagation using composite grids for classical scattering problems in two space dimensions. An analogous set of results in three space dimensions is now presented. Consider the diffraction of a plane wave incident on a perfectly conducting sphere of radius $R = 1$ embedded in an infinite dielectric media as illustrated in Figure 19. The incident field, denoted by $\mathbf{E}^I(\mathbf{x}, t)$, propagates in the positive $x-$direction and is taken to be

$$E_x^I = 0, \quad E_y^I = e^{i(k_x(x-ct))}, \quad E_z^I = 0. \tag{47}$$

For the computations, the infinite domain is truncated to a finite box with dimensions $[-3, 3] \times [-3, 3] \times [-3, 3]$. The composite grid used for this geometry consists of a background Cartesian grid together with three curvilinear patches which are used to represent the sphere as shown in Fig. 19 and also Fig. A.24 in Appendix A.4. This three-patch sphere is a high-quality grid and is chosen to avoid the polar singularities while providing near uniform grid spacing on the sphere surface. This can be seen in the center and right panels of Fig. 19. These images also indicate one of the primary differences between the 2D computations from Sections 6.1 and 6.2 and the current 3D studies in that grid interpolation on the geometry surface is encountered. This type of interpolation on physical boundaries is essentially ubiquitous in practical 3D computations using overlapping grids, and the ability of the upwind discretization to stabilize computations where interpolation points are near physical boundaries is therefore quite important. For more details on the grids see Appendix A.4. The exact time-harmonic solution is used for the initial conditions and to specify the field values on the exterior boundary of the box. The boundary conditions on the surface of the sphere are taken as those of a perfect electrical conductor (1b). Physical parameters for the computation are taken as $\epsilon = 1$, $\mu = 1$ and $k_x = 1$. As before, max-norm convergence studies for the second- and fourth-order accurate upwind schemes are performed, and the results reported in Table 3. The errors are observed to converge at close to the expected second- and fourth-order rates.

6.4. Scattering from a dielectric sphere

The final classical scattering problem considered is that of an incident plane wave (47) with wave number $k_x = 1$ impinging on a dielectric sphere of radius $R = 1$. A schematic of the problem is illustrated in Fig. 20.

2nd Order Max-norm Convergence												
h_j	E_x	r	E_y	r	E_z	r	$\partial_t E_x$	r	$\partial_t E_y$	r	$\partial_t E_z$	r
1/20	8.0e-2		1.0e-1		4.1e-2		4.9e-1		6.6e-1		2.8e-1	
1/40	1.4e-2	5.9	2.1e-2	4.8	8.7e-3	4.7	1.0e-1	4.7	1.5e-1	4.2	6.6e-2	4.2
1/80	2.4e-3	5.7	4.2e-3	5.0	2.0e-3	4.4	2.0e-2	5.2	3.4e-2	4.6	1.6e-2	4.3
rate		2.54		2.30		2.19		2.31		2.14		2.08
4th Order Max-norm Convergence												
h_j	E_x	r	E_y	r	E_z	r	$\partial_t E_x$	r	$\partial_t E_y$	r	$\partial_t E_z$	r
1/20	2.6e-2		4.2e-2		1.1e-2		2.8e-1		3.1e-1		9.0e-2	
1/40	1.5e-3	17.4	2.7e-3	15.2	7.3e-4	15.5	1.6e-2	18.2	2.1e-2	14.8	5.8e-3	15.7
1/80	7.3e-5	20.1	1.6e-4	17.5	4.2e-5	17.4	7.0e-4	22.2	1.2e-3	17.8	3.2e-4	17.8
rate		4.23		4.02		4.04		4.33		4.02		4.06

Table 3: Max-norm convergence study computing the scattered field from a conducting sphere using the second- and fourth-order-accurate schemes. The left-most column is the target grid spacing h_j. Columns labeled by field components contain errors computed at $t = .1$, and columns labeled r denote the ratio of errors for successive refinements. The two rows labelled *rate* show the computed average rate of convergence. Again the results show excellent agreement with the theoretically predicted convergence rates.

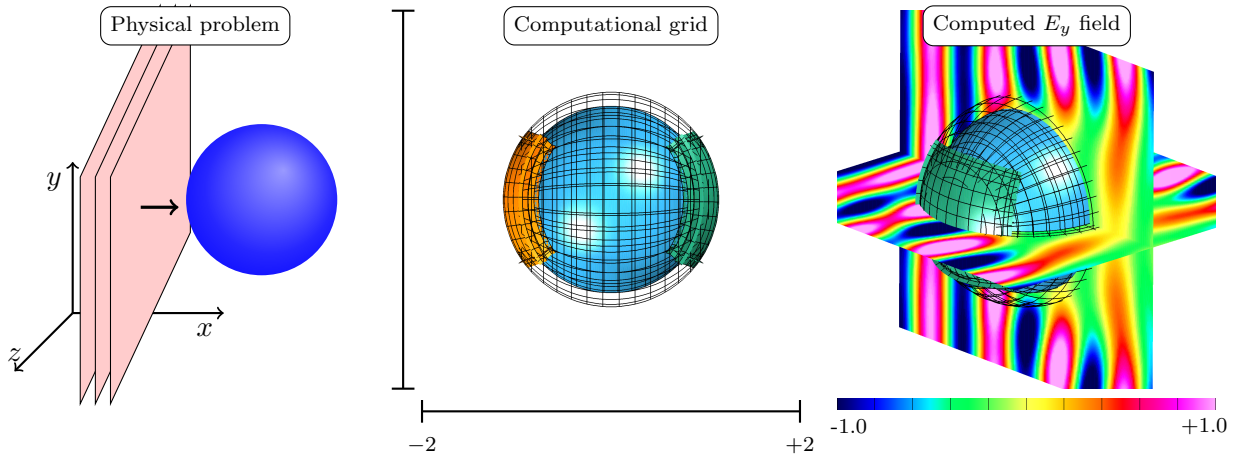

Figure 20: Left: Illustration of the scattering problem of a polarized plane wave impinging on dielectric sphere with $\epsilon = 0.25$. Middle: Overlapping grid construction for sphere, sphere interior, and truncated computational domain. Right: Computed E_y component and grid with approximate grid spacing $h_j \approx \frac{1}{80}$ and $k_x = 1$ at time $t = 0.25$. The overlapping solid sphere grid is coarsened for easier viewing.

Material properties for the interior of the sphere are taken as $\epsilon = 0.25$ and $\mu = 1$, while the properties for the region exterior to the sphere are $\epsilon = 1$ and $\mu = 1$. For the purposes of computation, the infinite computational domain is truncated to a box with dimensions $[-2, 2] \times [-2, 2] \times [-2, 2]$. The composite grids used for this two domain problem then consist of the composite grid previously discussed for scattering from a PEC sphere, together with a second composite grid for the interior problem. Each of the two composite grid structures is itself made of four component grids; three boundary fitted grids for the sphere along with and a background Cartesian grid. The surfaces of some of these grid patches are shown in Fig. 20. Additional details of the grid structure are provided in Appendix A.5. The interface conditions along the surface of the sphere are given by (1c), while initial conditions and boundary conditions on the outer boundary of the box are taken from the known exact solution. The results of convergence studies for this problem are presented in Table 4. There the max-norm errors for the second-order and fourth-order accurate upwind schemes are seen to converge at close to the expected second- and fourth-order rate. In addition, Fig. 21 shows plots of the three field components of the electric field $\mathbf{E}$, as well as the errors in these components at time $t = 0.25$. Here the solution is seen to be very smooth in the domain interiors, while the fields may jump at the material interface. Similarly, the errors show jumps at the material interfaces and a large degree of

2nd Order Max-norm Convergence												
h_j	E_x	r	E_y	r	E_z	r	$\partial_t E_x$	r	$\partial_t E_y$	r	$\partial_t E_z$	r
1/20	1.7e-2		2.8e-2		6.9e-3		2.0e-1		3.1e-1		9.0e-2	
1/40	3.9e-3	4.4	6.3e-3	4.4	1.7e-3	4.1	5.5e-2	3.5	8.5e-2	3.6	2.5e-2	3.7
1/80	9.4e-4	4.1	1.4e-3	4.4	4.0e-4	4.2	1.5e-2	3.6	2.1e-2	4.1	6.7e-3	3.7
rate		2.09		2.14		2.05		1.84		1.95		1.87
4th Order Max-norm Convergence												
h_j	E_x	r	E_y	r	E_z	r	$\partial_t E_x$	r	$\partial_t E_y$	r	$\partial_t E_z$	r
1/20	1.5e-3		5.8e-3		5.6e-4		2.2e-2		5.1e-2		8.8e-3	
1/40	9.4e-5	16.3	1.9e-4	29.6	3.6e-5	15.7	2.1e-3	10.9	3.1e-3	16.6	7.0e-4	12.5
1/80	6.1e-6	15.3	1.2e-5	15.6	2.2e-6	16.0	1.2e-4	16.8	1.8e-4	16.7	4.2e-5	16.8
rate		3.98		4.43		3.98		3.79		4.07		3.86

Table 4: Max-norm error convergence study from the computation of the scattered field from a dielectric sphere using the second-order and fourth-order accurate upwind schemes. The left-most column is the target grid spacing h_j. Columns labeled by field components contain errors computed at $t = .1$ and columns labeled r denote the ratio of errors for successive refinements. The two rows labeled *rate* show the computed average rate of convergence which show that the expected second- and fourth-order rates of convergence are convincingly demonstrated for all quantities.

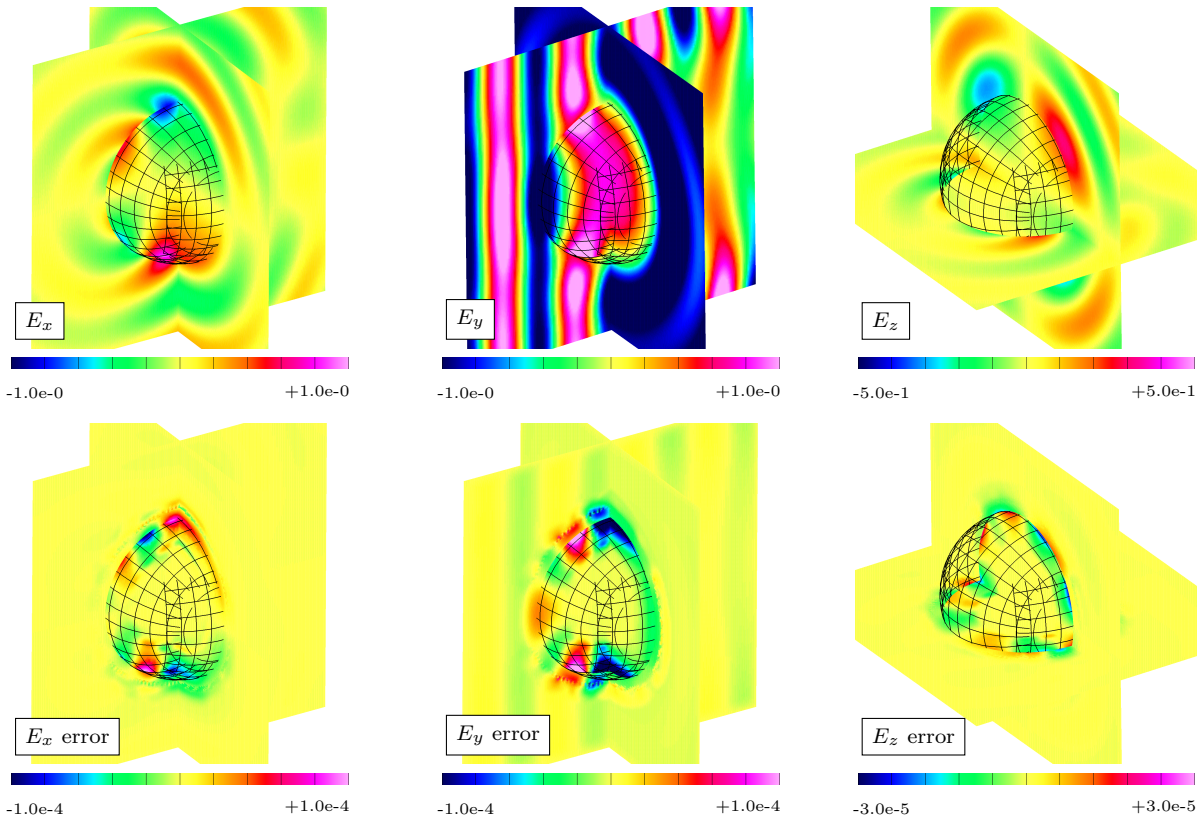

Figure 21: The solutions and errors for the scattering of a plane wave from a dielectric sphere at $t = 0.25$, with $k_x = 1$ computed using the fourth-order-accurate upwind scheme. Top row: Electric field components. Bottom row: Errors in the field components. The approximate grid spacing is $h \approx \frac{1}{80}$. The grid is coarsened for plotting.

smoothness on the domain interiors. However, in contrast to the 2D computations shown in Section 6.1, the interpolation boundaries are apparent in the error plots here due to the relative coarseness of the grids for these computations. Even still, the dominant errors are not associated with the interpolation boundaries.

Instead, the errors appear to be largest near the material interface and then decay toward the domain interior.

6.5. Scattering of a chirped plane wave from a conducting body embedded in a dielectric slab

A final more complex computational example relates to the challenging problem of using electromagnetic waves to detect a metal object buried just below the surface of the earth. The physical problem is illustrated in Fig. 22. In this setup, a *chirped* plane wave with linearly varying frequency is beamed from the upper air region toward the ground at some incident angle, and the resulting reflected wave is to be determined. The problem is formulated in two space dimensions with a rectangular shaped body buried below a planar material interface. The material properties for the upper *air* region are taken as $\epsilon_1 = 1$ and $\mu_1 = 1$, while those for the lower *ground* region are taken as $\epsilon_2 = 3$ and $\mu_2 = 1$.

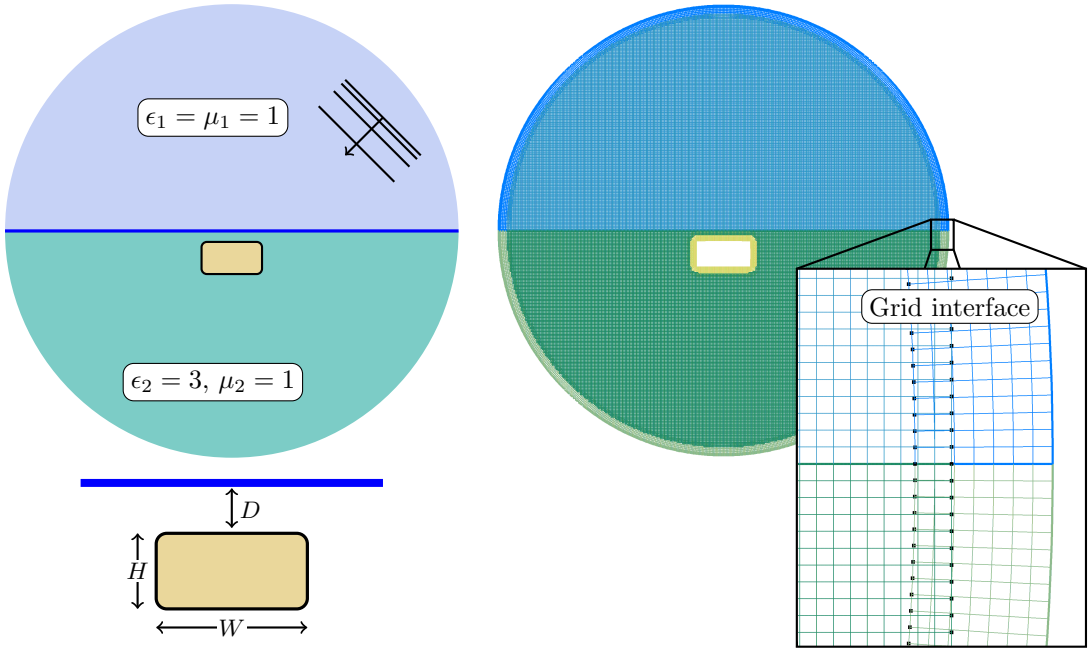

Figure 22: Scattering of a chirped plane wave from a buried conducting body. Top left: physical configuration with plane wave incident from the upper right in a region with material parameters ϵ_1 and μ_1. The conducting body is embedded in a material with parameters ϵ_2 and μ_2. Bottom left: the body, of width W and height H, lies a distance D below the interface. Right: composite grid for the configuration with a zoom of the grids near where the interface meets the far field boundary.

If the material surface of the dielectric is the plane $y = 0$, and the angle of incidence from the y-axis is θ then the incident field is of the form

$$\mathbf{E}^I(x,t) = \hat{\mathbf{a}}\ P\left(t - \xi_0 - \frac{\hat{\mathbf{k}}}{c}\cdot\mathbf{x}\right) = \hat{\mathbf{a}}\ P\left(\xi\right),$$

where P defines the wave-form with

$$\xi = t - \xi_0 - \frac{\hat{\mathbf{k}}}{c}\cdot\mathbf{x}, \quad \hat{\mathbf{a}} = (-\cos\theta,\ \sin\theta), \quad \hat{\mathbf{k}} = (-\sin(\theta),\ -\cos(\theta)), \quad \xi_0 = \frac{1}{2}(t_a + t_b),$$

and where $[t_a, t_b]$ represents the time interval when the wave source is radiating, and $c = 1/\sqrt{\epsilon_1\mu_1}$ is the speed of light in the upper air region. Note that $\hat{\mathbf{a}}\cdot\hat{\mathbf{k}} = \nabla\cdot\mathbf{E}^I = 0$. A linear chirp of unit amplitude and duration $\tau = t_b - t_a$ defines the waveform as

$$P(\xi) = \chi_\tau(\xi)e^{-i\phi(\xi)}, \quad \phi(\xi) = \omega_0\xi + \alpha\xi^2,$$

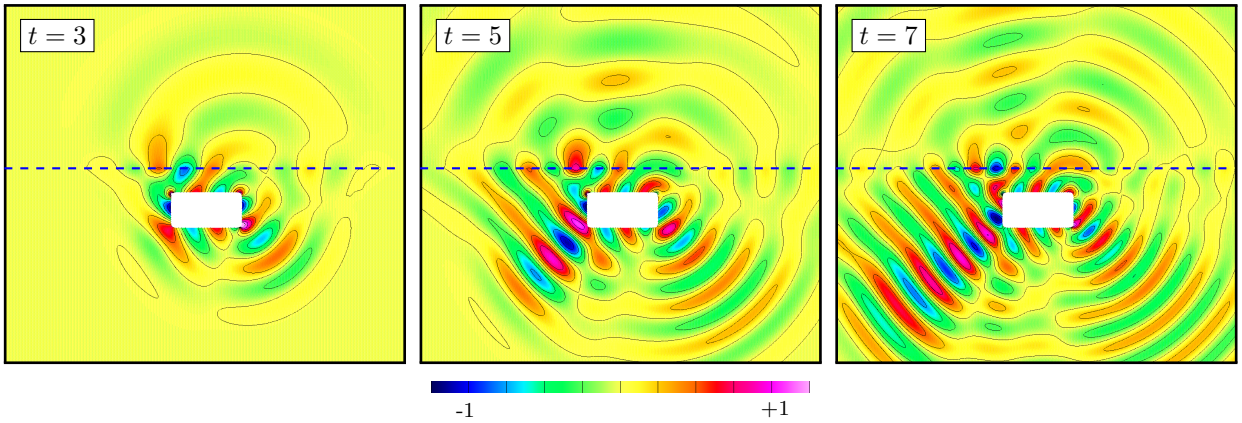

Figure 23: Scattering of a chirped plane wave from a conducting body embedded in a dielectric slab. The scattered E_x field is shown at the three times indicated in the plots. For clarity, the material interface is marked with a dashed line.

with a given carrier frequency ω_0, chirp rate $\alpha = \frac{B}{2\tau}$, bandwidth B, and where $\chi_\tau(t)$ is an indicator function used to turn the incident field on and off, defined here by the smoothed *top-hat* function,

$$\chi_\tau(\xi) = \frac{1}{2}\big(\tanh(\beta(\xi+\tau/2)) - \tanh(\beta(\xi-\tau/2))\big).$$

The "sharpness" of the indicator is determined by $\beta > 0$. Note that for large β, $\chi_\tau(\xi)$ approaches a *top-hat* function,

$$\chi_\tau(\xi) \approx \begin{cases} 1 & \text{for } \xi \in (-\tau/2, \tau/2), \\ 0 & \text{otherwise.} \end{cases}$$

Note also that the instantaneous frequency of the chirped incident field when $\chi_\tau(\xi) \approx 1$, is given by

$$\phi'(\xi) = \omega_0 + 2\alpha\xi = \omega_0 + \frac{B}{\tau}\xi,$$

and varies linearly over time. For this reason ϕ is said to define a *linear chirp*.

For reasons of efficiency, the scattered field is computed directly. This is accomplished by subtracting the solution to the related scattering problem with two regions but no embedded body. The solution for a regular plane wave impinging on a dielectric slab is well known [37], and the solution for the modulated chirped wave is of a similar form. For this case, the transmitted wave in the lower dielectric material is given by

$$\mathbf{E}^T = T\,\hat{\mathbf{a}}\,P\left(t - \xi_0 + \frac{x}{c_2}\sin(\theta_2) + \frac{y}{c_2}\cos(\theta_2)\right),$$

where $c_2 = 1/\sqrt{\epsilon_2\mu_2}$ is the wave speed in the lower dielectric slab, θ_2 is given by Snell's Law, and T is the transmission coefficient,

$$T = \frac{2\eta_1\cos\theta}{\eta_2\cos\theta + \eta_1\cos\theta_2}, \quad \eta_i = \sqrt{\frac{\mu_i}{\epsilon_i}}$$

which is the same as for a non-chirped waveform. In directly solving for the scattered field, $\mathbf{E}^S$, the conducting boundary condition on the embedded body becomes inhomogeneous,

$$\mathbf{n}\times\mathbf{E}^S = -\mathbf{n}\times\mathbf{E}^T,$$

which is easily incorporated into the numerical formulation.

The composite grid for the computational domain, which consists of five component grids, is shown in Fig. 22 (see also Fig. A.25 and the more detailed description of the grid construction in Appendix A.6). The embedded body is taken to have width $W = 1$ and height $H = 0.5$. The distance of the top of the

body to the interface at $y = 0$ is $D = 1/3$. Cartesian grids are used for the background of the upper and lower domains. Semi-circular annular grids cut the background domain into a circle and provide a far-field artificial boundary. Finally, a *smoothed polygon* is used to describe the boundary of the embedded body and a boundary-fitted grid is made by extending the normals from the body's boundary curve. Let $\mathcal{G}_{\rm eb}^{(j)}$ denote the composite grid for this configuration with resolution factor j which has a grid spacing of approximately $h_j = 1/(10j)$. Initial conditions for $\mathbf{E}$ and its time-derivative are set to zero, and the far field boundary conditions are taken to be a second-order Engquist Majda condition [40]. Fig. 6.5 shows the x-component of a scattered field at various times computed using the fourth-order accurate upwind scheme. The chirped wave boundary forcing turns on near $t_0 = 1$, and by time $t = 3$ the scattered field is seen to be propagating outward from the body. The wave fronts are seen to travel more quickly in the upper domain as expected.

The accuracy of the computed solution is assessed using a self-convergence grid refinement study. Simulations are performed with a sequence of composite grids of increasing resolution, and Richardson extrapolation is used to estimate the convergence rates and errors using the procedure described in [41, 42]. We have found that some care is required in performing this self-convergence study in order to demonstrate higher order accuracy. In particular, to avoid singularities associated with startup (e.g. turning the boundary forcing on impulsively leads to a discontinuous first derivative in the solution), the wave-form is chosen to *turn on* smoothly at $t_0 = 1$ and the parameter β in the indicator function is taken large enough so that the boundary forcing is below machine precision at $t = 0$, but not so large that its time variation is unresolved by the time-stepping scheme. Furthermore, to avoid pollution from reflections off the far-field boundary, the exterior boundaries are placed far from the embedded body, and the simulation is halted before large reflections from those boundaries could be observed. The following parameters are used for the grid refinement study:

ω_0	t_a	t_b	β	B	θ
$c\|k\|$	1	15	18	2	$\pi/3$

Using these choices, Table 6.5 shows the max-norm convergence results of this grid refinement study using the fourth-order accurate upwind scheme. The grids are $\mathcal{G}_{\rm eb}^{(j)}$, $j = 16$, 32 and 64 corresponding to approximate grid spacings of 1/160, 1/320 and 1/640, respectively. The estimate max-norm error convergence rates for $\mathbf{E}$ show some variation, and the average value of approximately 3.5 is considered to be in reasonably good agreement to the theoretically predicted rate, particularly for this fairly complex configuration.

h_j	E_x	r	E_y	r	H_z	r	$\partial_t E_x$	r	$\partial_t E_y$	r	$\partial_t H_z$	r
1/160	1.4e-2		1.6e-2		3.6e-4		5.4e-1		6.1e-1		3.0e-2	
1/320	1.4e-3	10.6	1.5e-3	11.1	2.6e-5	13.8	6.3e-2	8.7	6.5e-2	9.5	1.9e-3	16.0
1/640	1.3e-4	10.6	1.3e-4	11.1	1.9e-6	13.8	7.3e-3	8.7	6.9e-3	9.5	1.2e-4	16.0
rate		3.41		3.47		3.78		3.11		3.24		4.00

Table 5: Max-norm self convergence results for computing the scattered field from a conducting body in a dielectric slab using the fourth-order accurate upwind scheme. Errors estimated using Richardson extrapolation. The left-most column shows the target grid spacing h_j. Columns labeled by field components contain estimated errors computed at $t = 2$, and columns labeled r denote the ratio of estimated errors for successive refinements. The row labeled *rate* shows the computed average rate of convergence which is close to the expected rate.

7. Conclusions

We have presented a class of upwind scheme for the solution of time-dependent Maxwell's equations in their second-order form. The derivation of the schemes is performed in general curvilinear geometry using a conservative finite-difference approach. Formally exact, explicit, single-step formulae for field displacements and their time derivatives are presented. These differential difference formulae are expressed as an infinite expansion, and truncation to a finite number of terms yields discrete schemes of any desired order-of-accuracy. Upwinding is incorporated using an appropriate choice of the numerical flux function which embeds the exact solution to a generalized local Riemann problem.

The curvilinear formulation enables the use of overlapping composite grids to discretize the equations on complex domains, including multiple abutting materials. However, the schemes for general curvilinear

grids can be extremely costly in comparison to their optimized versions on Cartesian grids (more than an order of magnitude has been observed for 3D). Therefore for reasons of efficiency it is advantageous to fix the number of grid points in the normal direction to the boundary on any boundary fitted grids. Then as the computation is refined, the computational cost approaches the cost of solving only on the background Cartesian grids. It was shown in [21], and discussed again here, that this choice of thin boundary grids often excites strong instabilities for non-dissipative schemes. Also in [21] it was also shown that to recover stability, it suffices to add an artificial dissipation that scales proportional to the grid spacing, which ultimately costs an order of accuracy for a given stencil width. We have shown here that the upwind scheme effectively adds such a dissipation without any tunable parameters, and the schemes remain stable and fully accurate even when using thin boundary grids.

To understand this result theoretically, we have also presented a systematic stability analysis for the initial-boundary-value-problem on overlapping grids with a *fixed* number of grid points on the boundary grid. Normal mode analysis for the semi-discretization of the wave equation $u_{tt} = u_{xx}$ on a one-dimensional overlapping grid with a near boundary grid indicates that the upwind scheme is robust against perturbations typically introduced by grid interpolation. On the other hand, the analysis shows that instability is common for the non-dissipative scheme using the same grid configuration.

Finally, detailed numerical studies for electromagnetic scattering problems from perfect conductors and dielectrics using the full overlapping grid implementations for second- and fourth-order accuracy are presented. The computations illustrate the stability of the scheme on overlapping grids in two and three space dimensions, and the design accuracy of the codes is observed even when using thin boundary grids and measuring error in the difficult maximum-norm. A final more complex problem of scattering from a body embedded in a layered dielectric shows the robust nature of the scheme, and Richardson-style self-convergence again illustrates high-order accuracy.

There are many potential avenues for future work. For example, one could pursue a closed-form stability proof, and subsequently extend the stability analysis to higher orders of accuracy. From a computational perspective there are a number of optimizations that might be applied to improve the performance of the upwind scheme on curvilinear grids, which, due to it's larger stencil, is not as fast as the centered scheme. Finally, derivation of upwind-style discretizations for other wave equations in second-order form, such as linear or nonlinear elasticity, or Einstein's equations of general relativity, could be pursed.

Acknowledgements

Thanks are extended to Professor S. Tsynkov and Dr. A. Fedoseyev for discussions regarding the simulations in Section 6.5.

Appendix A. Computational grids

This appendix contains additional details of the component grids and composite overlapping grids used for the computations appearing in Section 5.1 and Section 6. This information is included for the purposes of aiding in the reproducibility of the results. In addition, input scripts which can be used with `ogen` grid generator are also available with `Overture` software releases, and can be used to generate all grids and subsequent numerical computations discussed in this manuscript.

Appendix A.1. Composite grid for a disk

The composite grid used in the computations of the eigenmodes of a disk in Section 5.1, as illustrated in Fig. 4, consists of a thin annular boundary fitted grid together with an interior Cartesian background grid. The annular grid with a fixed number of radial grid cells is defined by

$$\mathcal{A}([r_a, r_b], N_r, N_\theta(j)) = \Big\{ (r_{i_2}\cos(\theta_{i_1}), r_{i_2}\sin(\theta_{i_1})) \;\Big|\; r_{i_2} = r_a + i_2(r_b - r_a)/N_r,\ \theta_{i_1} = 2\pi i_1/N_\theta, \qquad (A.1)$$
$$i_1 = 0, 1 \ldots N_\theta(j),\ i_2 = 0, 1, \ldots, N_r \Big\},$$

and the interior background grid (rectangle) by

$$\mathcal{R}([x_a,x_b]\times[y_a,y_b],N_1,N_2)=\Big\{(x_a+i_1\Delta x_1,y_a+i_2\Delta x_2)\;\big|\;\Delta x_k=\frac{(x_b-x_a)}{N_k},\quad i_k=0,1,\ldots,N_k,\;\;k=1,2\Big\}. \tag{A.2}$$

The composite grid is then comprised of the union of these two component grids

$$\mathcal{G}^{(j)}=\mathcal{R}([-x_a,x_a]^2,N_x(j),N_x(j))\;\cup\;\mathcal{A}([r_a,r_b],N_r,N_\theta(j)),$$

where j denotes a grid resolution factor with grid spacing approximately given by $h_j=\frac{1}{10j}$. The grid parameters for a discrete upwind scheme of order m, with stencil width $2\lfloor\frac{m}{2}\rfloor+3$, requiring $N_{ghost}=\lfloor\frac{m}{2}\rfloor+1$ ghost cells are taken as

$$\begin{aligned}&r_a=1,\quad r_b=r_a-(N_r-1)h_j,\quad x_a=r_b+(N_{ghost}-1)h_j,\\ &N_x(j)=\left\lfloor\frac{2x_a}{h_j}+\frac{3}{2}\right\rfloor,\quad N_\theta(j)=\left\lfloor\frac{\pi(r_a+r_b)}{h_j}+\frac{3}{2}\right\rfloor,\end{aligned}$$

where the integer floor function $\lfloor x\rfloor$ denotes the largest integer less than x.

Appendix A.2. Composite grid for the exterior of a two-dimensional cylinder

The composite grid for the region exterior to a circular cylinder in two dimensions used in the computations of Section 6.1 for scattering from a PEC cylinder, and illustrated in Fig. 14, consists of an exterior Cartesian background grid along with an annular boundary fitted grid. The composite grid is defined as

$$\mathcal{G}_c^{(j)}=\mathcal{R}([-x_a,x_a]^2,N_x(j),N_x(j))\;\cup\;\mathcal{A}([r_a,r_b],N_r,N_\theta(j)), \tag{A.3}$$

where the square grid, $\mathcal{R}$, is defined by (A.2) and the annular grid, $\mathcal{A}$, is defined by (A.1). The grid parameters are

$$\begin{aligned}&x_a=2,\quad r_a=0.5,\quad r_b=r_a+(N_r-1)h_j,\\ &N_x(j)=\left\lfloor\frac{4}{h_j}+\frac{3}{2}\right\rfloor,\quad N_r=5+N_{ghost}+2(m-2),\quad N_\theta(j)=\left\lfloor\frac{\pi(r_a+r_b)}{h_j}+\frac{3}{2}\right\rfloor,\end{aligned}$$

and N_{ghost} is the number of ghost cells needed for a scheme of order m, given in Appendix A.1.

Appendix A.3. Composite grid for a dielectric disk embedded in a square domain

The composite grid for the two-dimensional regions interior and exterior to a circle used in the computations of Section 6.2 for scattering from a dielectric cylinder, and illustrated in Fig. 17, consists of four component grids. The exterior region is comprised of a square Cartesian grid and annular grid exterior to the disk surface. The interior region has an annular grid inside the disk surface and a Cartesian background grid to cover the disk interior. The composite grid, with target grid spacing $h_j=\frac{1}{20j}$, is constructed in terms of the previously defined component grids $\mathcal{R}$ and $\mathcal{A}$ as

$$\begin{aligned}\mathcal{G}_c^{(j)}=&\mathcal{R}([-X_a,X_a]^2,N_X(j),N_X(j))\;\cup\;\mathcal{A}([R_{inner},R_{outer}],N_R,N_\theta(j))\;\cup\\ &\mathcal{R}([-x_a,x_a]^2,N_x(j),N_x(j))\;\cup\;\mathcal{A}([r_{inner},r_{outer},N_r,N_\theta(j)).\end{aligned}$$

The grid parameters are given by

$$\begin{aligned}&X_a=1,\quad x_a=r_{inner}+h_j,\quad N_X(j)=\left\lfloor\frac{2}{h_j}+\frac{3}{2}\right\rfloor,\qquad N_x=\left\lfloor\frac{2x_a}{h_j}+\frac{3}{2}\right\rfloor,\\ &R_{inner}=0.4,\quad R_{outer}=R_{inner}+\Delta r,\quad r_{outer}=R_{outer},\quad r_{inner}=r_{outer}-\Delta r,\\ &\Delta r=(N_R(j)-1)h_j,\quad N_R=3+N_{ghost}+2(m-2),\quad N_\theta(j)=\left\lfloor\frac{2\pi r_{outer}}{h_j}+\frac{3}{2}\right\rfloor,\quad N_r=N_R.\end{aligned}$$

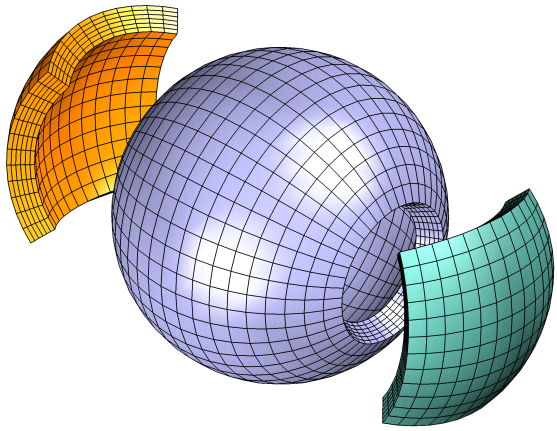

Figure A.24: Component grids for the sphere. The spherical polar patch $\mathcal{S}$ covers the main part of the sphere while the orthographic patches $\mathcal{O}_{\pm 1}$ cover the polar regions. The orthographic patches have been shifted outward for illustration purposes.

Appendix A.4. Composite grid for the region exterior to a sphere

The composite grid for the region exterior to a sphere, used in Section 6.3 for the scattering from a PEC sphere, and as illustrated in Fig. 19 consists of a Cartesian background grid together with three boundary-fitted curvilinear-patches for the sphere. The Cartesian box grid is defined by

$$\mathcal{B}([x_a,x_b]\times[y_a,y_b]\times[z_a,z_b],N_1,N_2,N_3)=\Big\{(x_a+i_1\Delta x_1,y_a+i_2\Delta x_2),z_a+i_3\Delta x_3)\;\Big|\;\Delta x_k=\frac{(x_b-x_a)}{N_k},\quad i_k=0,1,\ldots,N_k,\;\;k=1,2,3\Big\}. \tag{A.4}$$

The sphere is covered with a spherical-polar grid with the singular poles truncated, and two orthographic patches to cover the polar regions (the "three-patch" sphere grid) as shown in Fig. A.24. The polar grids are defined with the an orthographic transform,

$$\mathbf{x}=\mathbf{O}_p(\mathbf{r};[\rho_a,\rho_b],\hat{s}_2,\hat{s}_3)\equiv\left(p\frac{(1-\sigma^2)\rho}{1+\sigma^2},\frac{2\rho s_2}{1+\sigma^2},p\frac{2\rho s_3}{1+\sigma^2}\right) \tag{A.5}$$

where ρ, s_2, s_3 and σ are given in terms of the paramter space coordinates $\mathbf{r}=(r_1,r_2,r_3)\in[0,1]^3$ by

$$\rho=\rho_a+r_1(\rho_b-\rho_a),\qquad s_2=\left(r_2-\frac{1}{2}\right)\hat{s}_2,\qquad s_3=\left(r_3-\frac{1}{2}\right)\hat{s}_3,\qquad \sigma^2=s_2^2+s_3^2$$

with $p=1$ for the north pole and $p=-1$ for the south pole. Note that $[\rho_a,\rho_b]$ determine the radial extent while $\hat{s}_2$ and $\hat{s}_3$ determine the lateral extent. Finally, define the orthographic grid about pole p as,

$$\mathcal{O}_p([\varrho_a,\varrho_b],\hat{s}_2,\hat{s}_3,N_1,N_2,N_3)=\{\mathbf{x_i}\mid\mathbf{x_i}=\mathbf{O}_p(\mathbf{r_i};[\rho_a,\rho_b],\hat{s}_2,\hat{s}_3),\;\;i_\alpha=0,1,\ldots,N_\alpha,\;\;\alpha=1,2,3\}\,. \tag{A.6}$$

The spherical-polar grid, truncated at its poles, is defined by,

$$\begin{aligned}\mathcal{S}([\varrho_a,\varrho_b]\times[\theta_a,\theta_b]\times[\phi_a,\phi_b],N_1,N_2,N_3)=\{&(\varrho_{i_1}\cos\theta_{i_2}\sin\phi_{i_3},\varrho_{i_1}\sin\theta_{i_2}\sin\phi_{i_3},\varrho_{i_1}\cos\phi_{i_3})\mid\\ &\varrho_{i_1}=\varrho_a+i_1(\varrho_b-\varrho_a)/N_1,\theta_{i_2}=\theta_a+i_2(\theta_b-\theta_a)/N_2,\phi_{i_3}=\phi_a+i_3(\phi_b-\phi_a)/N_3,\\ &i_\alpha=0,1,\ldots,N_\alpha,\alpha=1,2,3\}.\end{aligned} \tag{A.7}$$

Finally, we can define the composite grid with grid spacing approximately $h_j=\frac{1}{10j}$ as,

$$\begin{aligned}\mathcal{G}_s^{(j)}=&\mathcal{B}([-2,2]^3,N_x(j),N_x(j),N_x(j))\;\cup\\ &\mathcal{O}_{\pm1}([R_{inner},R_{outer}],S_a,S_a,N_r,N_\theta(j),N_\theta(j))\;\cup\\ &\mathcal{S}([R_{inner},R_{outer}]\times[0,2\pi]\times[0.125\pi,0.875\pi],N_r,N_2(j),N_3(j)),\end{aligned}$$

with

$$R_{inner}=R,\quad R_{outer}=R_{inner}+(N_r-1)h_j,\quad S_a=0.65+(m-1)h_j,$$
$$N_x(j)=\left\lfloor 6/h_j+\frac{3}{2}\right\rfloor,\quad N_r=5+m,\quad N_\theta(j)=\left\lfloor 0.7^2\ \frac{\pi R}{h_j}+\frac{3}{2}\right\rfloor,$$
$$N_2(j)=\left\lfloor 0.7\frac{2\pi R}{h_j}+\frac{3}{2}\right\rfloor,\quad N_3(j)=\left\lfloor 0.85\frac{\pi R}{h_j}+\frac{3}{2}\right\rfloor,$$

for a scheme of order m and a sphere of radius R.

Appendix A.5. Composite grid for a dielectric sphere embedded in a box

The composite grid for the regions interior and exterior to a sphere, used in Section 6.4 for scattering from a dielectric sphere , and as illustrated in Fig. 20 consists of a total eight component grids. The region outside the sphere uses the four component grids, one Cartesian and the "three-patch" sphere grid, as described in Section Appendix A.4. The region interior to the sphere uses a similiar set of four component grids, a "three-patch" sphere grid and one interior background Cartesian grid. The composite grid is thus defined as

$$\begin{aligned}\mathcal{G}_{ss}^{(j)}=&\mathcal{B}([-X_a,X_a]^3,N_X(j),N_X(j),N_X(j))\ \cup\\ &\mathcal{S}([R_i,R_o]\times[0,2\pi]\times[.125\pi,.875\pi],N_R,N_\theta(j),N_\phi(j))\ \cup\\ &\mathcal{O}_{\pm1}([R_i,R_o],S_a,S_a,N_R,N_0(j),N_0(j))\ \cup\\ &\mathcal{B}([-x_a,x_a]^3,N_X(j),N_X(j),N_X(j))\ \cup\\ &\mathcal{S}([r_i,r_o]\times[0,2\pi]\times[.125\pi,.875\pi],N_r,N_\theta(j),N_\phi(j))\ \cup\\ &\mathcal{O}_{\pm1}([r_i,r_o],S_a,S_a,N_r,N_0(j),N_0(j)),\end{aligned}$$

with grid parameters for a scheme of order m given by

$$X_a=2,\quad x_a=(R_i+(m-2)h_j),\quad N_X(j)=\left\lfloor\frac{2X_a}{h_j}+\frac{3}{2}\right\rfloor,\quad N_x(j)=\left\lfloor\frac{2x_a}{h_j}+\frac{3}{2}\right\rfloor,$$
$$R_i=R,\quad R_o=R_i+(N_r-1)h_j,\quad r_o=R_i,\quad r_i=r_o-(N_r-1)h_j,\quad S_a=0.55+(m-1)h_j$$
$$N_r=3+m,\quad N_\theta(j)=\left\lfloor\frac{\pi R}{h_j}+\frac{3}{2}\right\rfloor,\quad N_\phi(j)=\left\lfloor\frac{\pi R}{2h_j}+\frac{3}{2}\right\rfloor,\quad N_0(j)=\left\lfloor 0.7S_a\frac{\pi R}{2h_j}+\frac{3}{2}\right\rfloor,$$

with a target grid spacing of $h_j=\frac{1}{10j}$.

Appendix A.6. Composite grid for a rectangular shaped body embedded in a dielectric slab

The composite grid, used in Section 6.5 for the simulation of a chirped plane wave impinging on a rectangular shaped body embedded in a dielectric slab, and shown in Figures 22 and A.25, covers an upper and lower region. The grid for the upper region consists of a Cartesian grid that covers the majority of the domain, together with a semi-circular annular grid for outer far-field boundary. The inner domain is also covered with a Cartesian and annular grid but in addition includes a body fitted curvilinear grid, denoted by $\mathcal{E}$, for the embedded body, see Fig. A.25. The curve for the surface of the rounded-rectangle is a *smoothed-polygon* mapping with rounded corners that is defined in terms of hyperbolic tangent functions as described in [43]. The rounding of the sharp corners allows a high quality grid to be generated near the corners which is important in resolving the numerical solution to Maxwell's equations in the vicinity of the corners. The sharpness of the corners can be adjusted, for all computations presented in this paper the sharpness parameter was taken to be 100. The composite grid for the upper and lower regions is defined by

$$\begin{aligned}\mathcal{G}^{(j)}=&\mathcal{R}([x_a,x_b]\times[y_a,y_b],N_x(j),N_y(j))\ \cup\ \mathcal{A}([r_a,r_b]\times[\theta_a,\theta_b],N_r,N_\theta(j))\ \cup\\ &\mathcal{R}([x_a,x_b]\times[Y_a,Y_b],N_x(j),N_Y(j))\ \cup\ \mathcal{A}([r_a,r_b]\times[\Theta_a,\Theta_b],N_r,N_\Theta(j))\ \cup\ \mathcal{E}(N_{r_b},N_{\theta_b}(j)).\end{aligned}$$

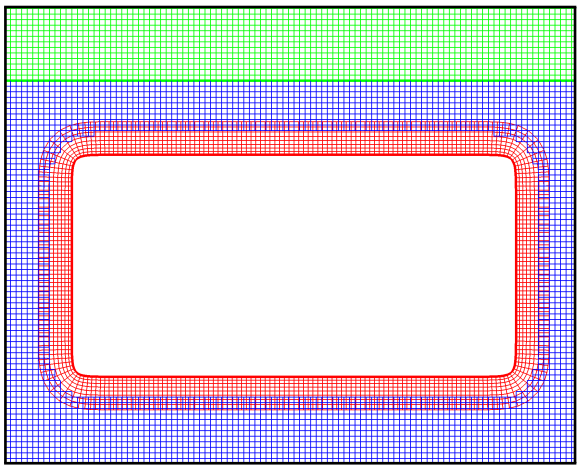

Figure A.25: A smoothed polygon mapping (in red) is used to represent the rectangular-shaped body with smoothed corners. The high-quality grid near the rounded corners is used to accurately resolve the numerical solution which can vary rapidly in the vicinity of the corners.

The grid parameters are

$$
\begin{aligned}
&x_a = -4, \quad x_b = 4, \quad y_a = 0, \quad y_b = 4, \quad Y_a = -4, \quad Y_b = 0, \quad r_b = x_b, \quad r_a = r_b - h_j N_r(j), \\
&\theta_a = 0, \quad \theta_b = \pi, \quad \Theta_a = \pi, \quad \Theta_b = 2\pi, \\
&N_x(j) = \left\lfloor \frac{x_b - x_a}{h_j} + \frac{3}{2} \right\rfloor, \quad N_y(j) = \left\lfloor \frac{y_b - y_a}{h_j} + \frac{3}{2} \right\rfloor, \quad N_Y(j) = \left\lfloor \frac{Y_b - Y_a}{h_j} + \frac{3}{2} \right\rfloor, \\
&N_r = N_r^0 + N_{ghost}, \quad N_\theta(j) = \left\lfloor \frac{\pi(r_a + r_b)}{h_j} + \frac{3}{2} \right\rfloor, \quad N_\Theta(j) = N_\theta(j).
\end{aligned}
$$

where $h_j = \frac{1}{10j}$ is the target grid spacing and N_{ghost} is the number of ghost cells.

References

[1] J. W. Banks, W. D. Henshaw, Upwind schemes for the wave equation in second-order form, J. Comput. Phys. 231 (17) (2012) 5854–5889.

[2] W. D. Henshaw, A high-order accurate parallel solver for Maxwell's equations on overlapping grids, SIAM J. Sci. Comput. 28 (5) (2006) 1730–1765.

[3] K. S. Yee, Numerical solution of initial boundary value problems involving Maxwell's equations in isotropic media, IEEE T. Antenn. Propag. 14 (3) (1966) 302–307.

[4] J. Nédélec, Mixed finite elements in $\mathcal{R}^3$, Numer. Math. 35 (3) (1980) 315–341.

[5] R. Courant, E. Isaacson, M. Rees, On the solution of nonlinear hyperbolic differential equations by finite differences, Commun. Pur. Appl. Math. 5 (1952) 243–255.

[6] S. K. Godunov, Finite difference method for numerical computation of discontinuous solutions of the equations of fluid dynamics, Mat. Sb. 47 (1959) 271–306.

[7] J. P. Boris, D. L. Book, Flux-corrected transport. I. SHASTA, a fluid transport algorithm that works, J. Comput. Phys. 11 (1973) 38–69.

[8] M. Shoucri, G. Knorr, Numerical integration of the Vlasov equation, J. Comput. Phys. 14 (1) (1974) 84–92.

[9] C. Z. Cheng, G. Knorr, The integration of the Vlasov equation in configuration space, J. Comput. Phys. 22 (3) (1976) 330–351.

[10] A. Robert, A semi-lagrangian and semi-implicit numerical integration scheme for the primitive meteorological equations, Journal of the Meteorological Society of Japan. Ser. II 60 (1) (1982) 319–325.

[11] P. Colella, P. R. Woodward, The piecewise parabolic method (PPM) for gas-dynamical simulations, J. Comput. Phys. 54 (1) (1984) 174–201.

[12] A. Harten, B. Engquist, S. Osher, S. Chakravarthy, Uniformly high order accurate essentially non-oscillitory schemes, III, J. Comput. Phys. 71 (1987) 231–303.

[13] C.-W. Shu, S. Osher, Efficient implementation of essentially non-oscillatory shock-capturing schemes, J. Comput. Phys. 77 (2) (1988) 439–471.

[14] B. Cockburn, C. W. Shu, TVB Runge-Kutta local projection discontinuous Galerkin finite-element method for conservation-laws 2: general framework, Math. Comput. 52 (1989) 411–435.

[15] G.-S. Jiang, C.-W. Shu, Efficient implementation of weighted ENO schemes, J. Comput. Phys. 126 (1) (1996) 202–228.

[16] R. Christensen, Godunov methods on a staggered mesh - an imporved artificial viscosity, Research Report UCRL-JC-105269, Lawrence Livermore National Laboratory (1990).

[17] R. D. Richtmyer, Proposed numerical method for calculation of shocks, Tech. Rep. LA-671, Los Alamos National Laboratory (1948).

[18] R. D. Richtmyer, Proposed numerical method for calculation of shocks, II, Tech. Rep. LA-699, Los Alamos National Laboratory (1948).

[19] J. VonNeumann, R. D. Richtmyer, A method for the numerical calculation of hydrodynamic shocks, J. Appl. Phys. 21 (1950) 232–243.

[20] J. W. Banks, W. D. Henshaw, High-order upwind methods for wave equations on curvilinear and overlapping grids, in: Spectral and High Order Methods for Partial Differential Equations - ICOSAHOM 14, Vol. 107 of Lecture Notes in Computational Science and Engineering, Springer, 2015, pp. 137–145.

[21] D. Appelö, J. W. Banks, W. D. Henshaw, D. W. Schwendeman, Numerical methods for solid mechanics on overlapping grids: Linear elasticity, J. Comput. Phys. 231 (2012) 6012–6050.

[22] D. Appelö, T. Hagstrom, A new discontinuous Galerkin formulation for wave equations in second-order form, SIAM Journal on Numerical Analysis 53 (6) (2015) 2705–2726.

[23] J. S. Hesthaven, High-order accurate methods in time-domain computational electromagnetics: A review, Advances in imaging and electron physics 127 (2003) 59–123.

[24] A. Taflove, S. C. Hagness, Computational Electrodynamics: The Finite-Difference Time-Domain Method, Artech House, 2000.

[25] G. C. Cohen, Higher-Order Numerical Methods for Transient Wave Equations, Springer, New York, 2002.

[26] T. A. Driscoll, B. Fornberg, Block pseudospectral methods for Maxwell's equations II: Two-dimensional, discontinuous coefficients case, SIAM J. Sci. Comput. 21 (3) (1999) 1146–1167.

[27] H.-O. Kreiss, Stability theory of difference approximations of mixed initial boundary value problems. I, Mathematics of Computation 22 (1968) 703–714.

[28] B. Gustafsson, H.-O. Kreiss, A. Sundström, Stability theory of difference approximations for mixed initial boundary value problems. II, Mathematics of Computation 26 (119) (1972) 649–686.

[29] G. Chesshire, W. Henshaw, Composite overlapping meshes for the solution of partial differential equations, J. Comput. Phys. 90 (1990) 1–64.

[30] B. Fornberg, A Practical Guide to Pseudospectral Methods, Cambridge University Press, Cambridge, 1996.

[31] B. Gustafsson, H.-O. Kreiss, J. Oliger, Time Dependent Problems and Difference Methods, John Wiley & Sons, New York, 1995.

[32] W. D. Henshaw, D. W. Schwendeman, An adaptive numerical scheme for high-speed reactive flow on overlapping grids, J. Comput. Phys. 191 (2) (2003) 420–447.

[33] J. C. Strikwerda, Initial boundary value problems for the method of lines, Journal of Computational Physics 34 (1) (1980) 94 – 107.

[34] B. Buchberger, Gröbner-Bases: An Algorithmic Method in Polynomial Ideal Theory., Reidel Publishing Company, Dodrecht - Boston - Lancaster, 1985.

[35] T. Y. Li, Numerical solution of multivariate polynomial systems by homotopy continuation methods, Acta Numerica 6 (1997) 399–436.

[36] J. Verschelde, Polynomial homotopy continuation with PHCpack (2010).

[37] C. A. Balanis, Advanced Engineering Electromagnetics, John Wiley & Sons, 1989.

[38] J. J. Bowman, T. B. A. Senior, P. L. E. Uslenghi, Electromagnetic and Acoustic Scattering by Simple Shapes, John Wiley and Sons, Hemisphere Publishing Corporation, 1996.

[39] H. C. van de Hulst, Light Scattering by Small Particles, Dover Publications, Inc., 1957.

[40] B. Engquist, A. Majda, Absorbing boundary conditions for numerical simulation of waves, Proceedings of the National Academy of Sciences 74 (5) (1977) 1765–1766.

[41] W. D. Henshaw, D. W. Schwendeman, Parallel computation of three-dimensional flows using overlapping grids with adaptive mesh refinement, J. Comput. Phys. 227 (16) (2008) 7469–7502.

[42] J. W. Banks, W. D. Henshaw, J. N. Shadid, An evaluation of the FCT method for high-speed flows on structured overlapping grids, J. Comput. Phys. 228 (15) (2009) 5349–5369.

[43] W. D. Henshaw, Mappings for Overture, a description of the Mapping class and documentation for many useful Mappings, Research Report UCRL-MA-132239, Lawrence Livermore National Laboratory (1998).